Initiation and propagation of strain localization in circumferentially notched samples of two porous sandstones

Sheryl Tembe,[1] Veronika Vajdova,[1,2] Teng-fong Wong,[1] and Wei Zhu[1]

[1] To investigate how strain localization develops from a structural and stress heterogeneity, we introduced a V-shaped circumferential notch in cylindrical samples of Bentheim and Berea sandstones and conducted triaxial compression tests at confining pressure optimum for compactive failure. The critical stresses for initial yield map out a cap with a negative slope in the stress space, and the presence of the notch enhanced the local stress which induced damage to occur at remote stresses significantly lower than in the unnotched sample. Our mechanical and microstructural data demonstrate the spectrum of failure modes and depict the initiation and propagation of a localized structure. In the Bentheim sandstone we observed discrete compaction bands that propagated through the sample cross section with episodic force drops, and in the Berea sandstone, we observed diffuse bands accompanied by strain hardening. Compactive yield was marked by an upsurge in acoustic emissions, corresponding to the formation of a process zone at the notch tip. To probe the initial yield behavior and geometry of the process zone, we developed a micromechanical model using linear elastic fracture mechanics, which predicts a process zone extending $0.3-0.5$ of the notch depth, in accord with the microstructural observations. Analysis of the stress path reveals the potential activation of multiple localization modes around the notch tip. The energy required to develop a compactive deformation band was inferred to range from 6 to 43 kJ m^{-2}. In the Bentheim sandstone the energy was observed to be inversely dependent on the confining pressure.

1. Introduction

[2] The coupled development of compaction and strain localization may significantly impact the stress field and strain partitioning in tectonic settings. Laboratory studies on porous sandstones have demonstrated that compaction localization is an important failure mode, particularly at stress states associated with the transition from brittle faulting to cataclastic flow [*Olsson*, 1999; *DiGiovanni et al.*, 2000; *Olsson and Holcomb*, 2000; *Wong et al.*, 2001]. Furthermore such a localized failure mode is accompanied by significant permeability reduction [*Holcomb and Olsson*, 2003; *Sternlof et al.*, 2004; *Vajdova et al.*, 2004].

[3] *Baud et al.* [2004] recently investigated five sandstones with porosities ranging from 13% to 25%, and their observations underscore the geometric complexity associated with such localization phenomena. They distinguished two end-members: shear bands at relatively high angles, and arrays of discrete compaction bands subperpendicular to the maximum compression (σ_1) direction, which were observed in the most compact and porous sandstones, respectively. While many structural attributes of discrete compaction bands observed in the laboratory are similar to bands observed in the field [*Mollema and Antonellini*, 1996; *Sternlof et al.*, 2004], there are some differences in the boundary conditions. In a laboratory sample a discrete band seems to propagate unstably and cut through the cross section of the sample, manifested by episodic stress drops and surges of acoustic emission (AE) activity. The bands tend to first appear as discrete entities clustered at either ends, and further deformation was then accommodated by the development of many more bands distributed throughout the sample. The first bands were possibly triggered by the local stress heterogeneity due to the end constraints of a laboratory sample. Since in the field local heterogeneities are pervasive on all scales, a deeper understanding of how they control the initiation of compaction localization necessitates studying the process under well-defined conditions of stress concentration.

[4] In a first attempt to investigate how a stress concentration controls compaction band development, *Vajdova and Wong* [2003] conducted triaxial compression experiments

[1]Department of Geosciences, State University of New York at Stony Brook, Stony Brook, New York, USA.
[2]Now at ReedHycalog, Houston, Texas, USA.

Table 1. Petrophysical Properties of the Two Sandstones Investigated in This Study

Sandstone	Porosity, %	Grain Diameter, mm	Composition
Bentheim	22.8	0.20	quartz 95%, kaolinite 5%
Berea	21.0	0.26	quartz 75%, feldspar 10%, carbonates 5%, clay ~10%

on circumferentially notched samples of Bentheim sandstone. Unlike the scenario in an unnotched specimen they observed that discrete compaction bands initiated from the notch tips and propagated by sequential increments along a path subperpendicular to the σ_1 direction. Furthermore the initiation of compaction localization from the notch tip was marked by an upsurge of AE activity, at a nominal stress appreciably lower than that required for compactive yield to initiate in an unnotched sample.

[5] *Vajdova and Wong*'s [2003] study opens up a number of fundamental questions on the initiation and propagation of compaction localization that we would also address in this study. They conducted experiments at a single confining pressure. To what extent are their observations reproduced at lower and higher pressures? Are the yield stresses for the initiation of compactive yield at the notch tip dependent on pressure? Given the broad spectrum of localization modes predicted by bifurcation analysis [*Issen and Rudnicki*, 2000] and documented experimentally in different sandstones [*Baud et al.*, 2004] it seems likely that the behavior observed by *Vajdova and Wong* [2003] in notched samples of Bentheim sandstone corresponds to one end-member. How are the initiation and propagation behaviors different in other porous sandstones? *Vajdova and Wong* [2003] observed that at a pressure of 300 MPa the propagation of a compaction band in Bentheim sandstone involved relatively high energy on the order of 10 kJ m^{-2}. Are the energetics for propagation of compaction localization similar in other sandstones under different pressures? To extrapolate the laboratory data to field settings, it is necessary to have a basic understanding of the stress field in the proximity of the notch tip and its influence on the localization behavior. In fracture mechanics the notched configuration has been used widely. How can some of these fracture mechanics analyses originally developed for tensile loading be modified to interpret the mechanical response for compressive loading, and what insights can we gain on the role of the compactive stress concentration? The present study was undertaken to address these questions.

2. Experimental Methodology

2.1. Sandstones Studied

[6] We investigate the localization behavior of two sandstones, the Bentheim and the Berea. The Bentheim sandstone samples (with initial porosity of 23% and average grain diameter of 0.2 mm) are from the same block used by *Vajdova and Wong* [2003] and *Wong et al.* [2001]. The Berea sandstone samples (with initial porosity of 21% and average grain diameter 0.26 mm) are from the block used by *Baud et al.* [2004] and *Wong et al.* [1997]. A petrophysical description is provided in Table 1. Both sandstones were cored perpendicular to bedding with sample dimensions of

diameter D = 18.4 mm and length 38.1 mm. A V-shaped notch was machined along the circumference of the mid-section, to give a minimum diameter of d = 14.4 mm (Figure 1).

2.2. Mechanical Deformation and Acoustic Emission

[7] The mechanical measurements were conducted in the conventional triaxial configuration (with the compressive principal stresses given by $\sigma_1 > \sigma_2 = \sigma_3$) following methodology detailed previously [*Wong et al.*, 1997; *Vajdova and Wong*, 2003]. The notched sample was jacketed with a thin copper foil and then with polyolefine tubing. The nominally dry samples were deformed at confining pressures of 250, 300, and 350 MPa for the Bentheim and 150, 200, and 250 MPa for the Berea, with a servo-controlled axial displacement rate of 0.5 μm/s. After accounting for the elastic deformation of the loading system and normalizing the sample displacement by the nominal length, this fixed displacement rate corresponds to a nominal axial strain rate of 1.0×10^{-5} s^{-1}. Volumetric strain was not monitored since strain gauges could not be applied to the notch surface.

[8] To record AE activity during triaxial experiments, we used a piezoelectric transducer (PZT-7, 5 mm diameter, 1 MHz longitudinal resonant frequency) mounted on the flat surface of one of the end plugs attached to the jacketed sample. The AE signals were conditioned by a preamplifier and to distinguish AE events from electric noise, a discriminator was used to check the amplitude and oscillational characteristics of the incoming signal [*Zhang et al.*, 1990b].

[9] The confining pressure P_c was applied first to the boundaries (cylindrical surface and two flat ends) of the jacketed sample and notch. The sample at this stage is considered to be uniformly stressed. However, a heterogeneous stress field would develop subsequently if additional axial force was applied to the sample ends. The axial force F is partitioned between the component $(\pi D^2/4)P_c$ (which contributes to a uniform hydrostatic stress field in the notched sample), and the differential force $F - (\pi D^2/4)P_c$
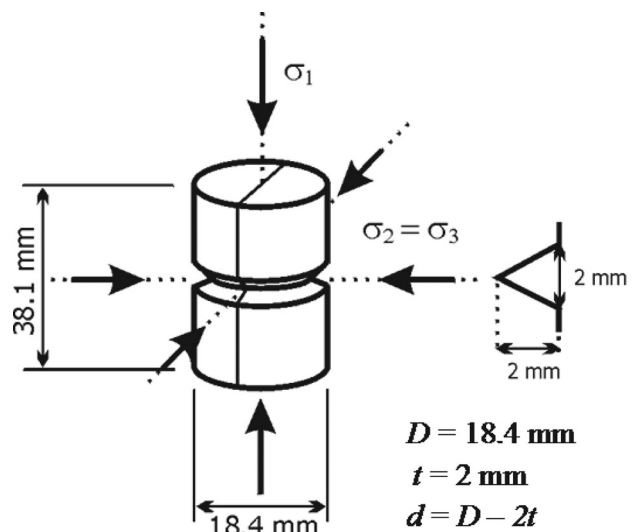

Figure 1. Geometric configuration of a notched sample loaded in a conventional triaxial apparatus.

Table 2. Initial Yield Stresses for Notched Samples of Bentheim and Berea Sandstone in Terms of the Nominal Axial, Nominal Mean, and Nominal Differential Stresses σ_o, P_o, and Q_o, Respectively[a]

| Sample | P_c, MPa | Nominal Stresses at Initial Yield | | | Stage of Deformation |
		σ_o, MPa	P_o, MPa	Q_o, MPa	
Bentheim					
BN9	250	363	288	113	3
BN3	300	390	330	90	1
BN4	300	408	336	108	1
BN7	300	395	332	95	1
BN2	300	410	337	110	2
BN5	300	403	334	103	2
BN6	300	407	336	107	2
BN1	300	399	333	99	3
BN8	350	417	372	67	3
Berea					
BR2	150	314	204	164	3
BR6	200	355	252	155	1
BR5	200	360	253	160	2
BR1	200	353	251	153	3
BR3	250	376	292	126	3

[a]These stresses are determined at the point of deviation from nonlinearity in the force-displacement curve. They do not correspond to the stresses attained at the end of the experiment. The Bentheim sandstone data for P_c = 300 MPa are from *Vajdova and Wong* [2003].

that induces a heterogeneous field with stress concentration near the notch tip. We will normalize these forces with respect to the nominal area, and refer to $\sigma_o = F/(\pi D^2/4)$ as the "nominal axial stress", $Q_o = F/(\pi D^2/4) - P_c = \sigma_o - P_c$ as "nominal differential stress" and $P_o = (\sigma_o + 2P_c)/3$ as "nominal mean stress", respectively. In the absence of the notch these nominal stresses would be identical to the principal stress σ_1, differential stress $Q = \sigma_1 - \sigma_3$ and mean stress $P = (\sigma_1 + 2\sigma_3)/3$ for an intact sample. We will also adopt the sign convention that the compressive stresses and compactive strains are positive.

2.3. Microstructural Observation

[10] The deformed samples were impregnated with epoxy and then sawed along a plane parallel to the axial direction to prepare thin sections. Optical microscopy was performed on 14 thin sections of the failed samples (Table 2) using a Nikon petrographic microscope in reflected light. Detailed observations of damage in selected samples were performed on thin sections sputter coated with 3 nm of gold using a LEO 1550 scanning electron microscope (SEM). SEM micrographs were acquired as backscattered electron images at a voltage of 15 kV. Up to 100 SEM images would be incorporated into a mosaic to map out the spatial distribution of damage in the vicinity of a notch.

3. Mechanical Deformation and Failure Mode in Notched Samples

[11] The inelastic and failure behavior of porous sandstones falls between the two end-members of dilatant brittle faulting and cataclastic flow. In the transitional regime the recent observations of *Baud et al.* [2004] have revealed a broad spectrum of geometric attributes that are associated with compactant failure. We will follow their terminology in

our latter discussion, where (1) a localized structure that is subperpendicular to the maximum principal stress σ_1 will be referred to as a "compaction band", whereas a localized structure that subtends a relatively high angle (say $45°–80°$) to σ_1 will be referred to as a "high-angle shear band," and (2) a localized structure that extends laterally over only a few (say 3) grains will be referred to as a "discrete band", whereas a structure that extends laterally over many grains will be referred to as a "diffuse band". High-angle shear bands commonly develop as conjugate sets of diffuse bands. A compaction band may be discrete or diffuse and while discrete compaction bands commonly develop as a subparallel array, a diffuse compaction band accommodates the cumulative strain by lateral propagation of damage.

[12] Unnotched samples of Bentheim and Berea sandstone show a wide range of failure modes, which can be mapped out in the stress space in relation to the peak stress for dilatant faulting and yield stress for the onset of shear-enhanced compaction [*Baud et al.*, 2004]. The latter can be determined by comparing the data for porosity reduction as a function of mean stress in a triaxial test and hydrostatic test. The stress state *C** at which the triaxial curve deviates from the hydrostat with a measurable contribution of inelastic porosity change induced by the deviatoric stress marks the onset of shear-enhanced compaction. In a plasticity model for porous rock laboratory measurements of *C** provide values of the initial yield stress [*Wong et al.*, 1997]. The critical stress states for the unnotched samples of Bentheim sandstone are given in terms of the mean stress P and differential stress Q in Figure 2a and in terms of the effective mean stress (which is simply the mean stress P less the pore pressure p_p) and differential stress Q in Figure 2b for the Berea sandstone. While under low confinement, dilatant faulting (open squares) is observed in both sandstones, the two show very different failure modes at higher effective pressures. Bentheim sandstone has a dominant failure mode of discrete compaction bands that is observed in both dry and wet experiments. In the Berea sandstone strain localization (involving high-angle conjugate shears or diffuse compaction bands) occurs within a relatively narrow pressure range, above which strain localization is inhibited and compactive failure develops by distributed cataclastic flow [*Menéndez et al.*, 1996].

[13] It should be noted that the observations of *Baud et al.* [2004] summarized in Figure 2a were for dry Bentheim sandstone samples whereas those in Figure 2b were for saturated Berea sandstone samples deformed with 10 MPa of pore pressure. Since this study focuses on dry samples, we include in Figure 2b (as solid circles) the yield stress data for dry Berea sandstone reported by *Baud et al.* [2000]. It would have been preferable to also show in Figure 2b the failure modes for dry Berea sandstone, but we are not aware of such observations that are as comprehensive as those of *Baud et al.* [2004] for wet Berea sandstone. Mechanical data and observations reviewed by *Wong et al.* [1997] indicate that failure modes for dry and wet Berea sandstone are qualitatively similar under comparable pressure conditions, although the strengths and yield stresses are somewhat lower in the wet samples [*Baud et al.*, 2000].

[14] Guided by these mechanical data and microstructural observations on unnotched samples, we deformed circumferentially notched samples of each sandstone at confining
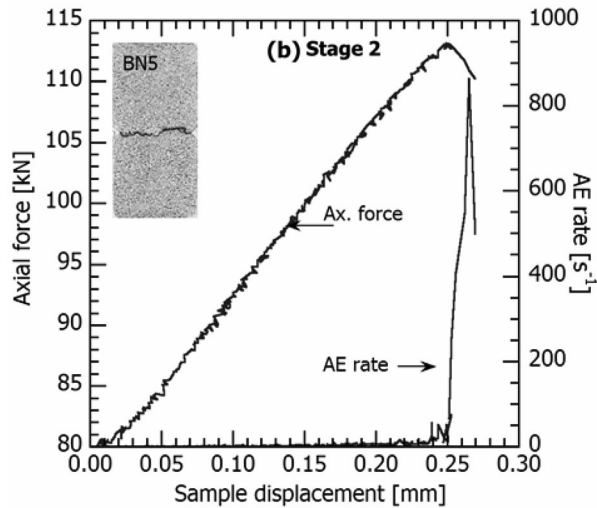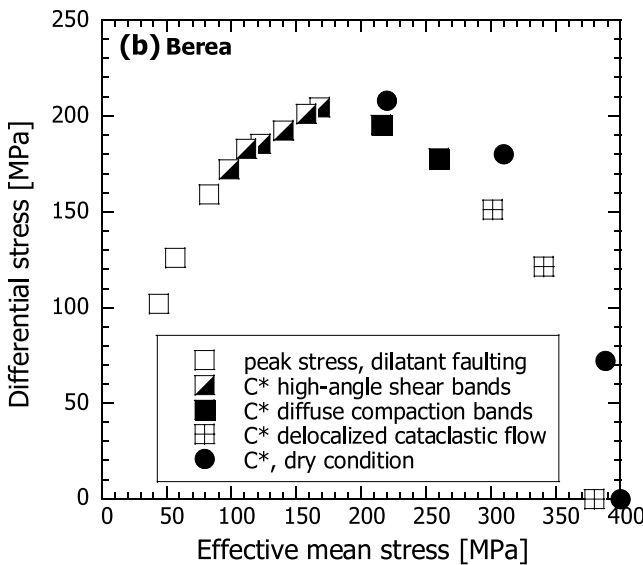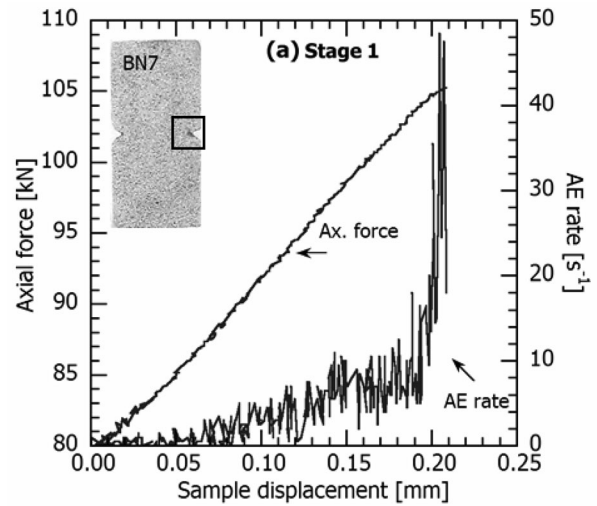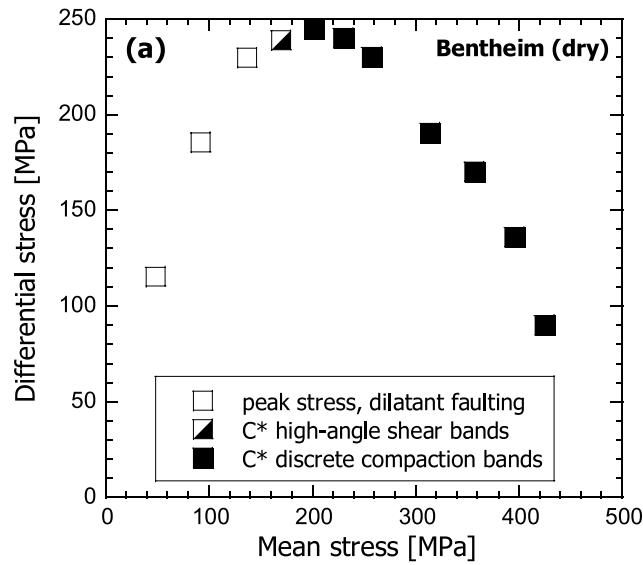
Figure 2. Critical stresses for the onset of shear-enhanced compaction C* and brittle strengths for unnotched samples of (a) dry Bentheim [*Klein et al.*, 2001; *Baud et al.*, 2004] and (b) wet Berea sandstones [*Menéndez et al.*, 1996; *Baud et al.*, 2004]. Data for dry Berea sandstone from *Baud et al.* [2000] are also shown. The associated failure modes are also indicated.
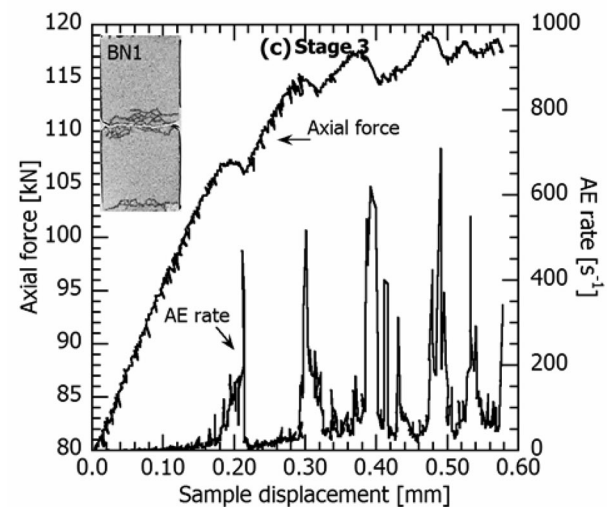
Figure 3. Axial force applied at the sample ends and AE rate as functions of axial displacement at 300 MPa confining pressure for notched samples of dry Bentheim sandstone loaded to various stages of compaction band development: (a) initial yield, (b) full extension of a discrete band, and (c) a subparallel array of discrete bands. The insets are thin sections of the full sample where damage appears as dark bands clustering at the notch tips. The rectangle marks the section of sample BN7 shown in detail in Figure 9b.
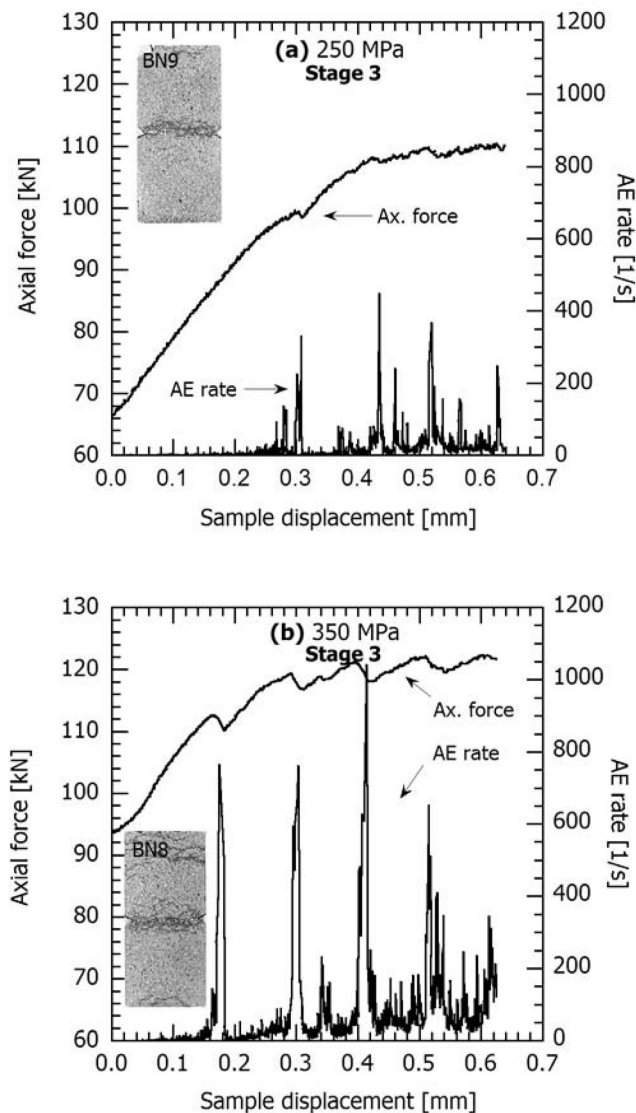
Figure 4. Axial force applied at the sample ends and AE as a function of axial displacement for notched samples of dry Bentheim sandstone deformed to stage 3 at confining pressures: (a) 250 MPa and (b) 350 MPa. Insets are thin sections of the deformed sample that show a developed array of discrete compaction bands at the notch.

pressures optimum for the different localization modes to develop.

3.1. Bentheim Sandstone: Influence of Pressure on Yield Stress and Failure Mode

[15] At a confining pressure of 300 MPa, *Vajdova and Wong* [2003] identified three stages of failure development in notched Bentheim sandstone, associated with distinct signatures of inelastic behavior and AE activity. For reference, in Figure 3 we show their mechanical and AE data for each stage, with thin sections of deformed samples as insets to illustrate the associated failure modes. Initially the displacement of a notched sample increased linearly with axial force, and termination of this first stage was signaled by an appreciable increase of AE activity (Figure 3a). In the

deformed sample (BN7) a highly localized damage zone was observed in the proximity of the notch. In the second stage the AE rate continued to increase while the displacement increased nonlinearly with axial force, until the force attained a peak and this stage terminated with a small force drop (Figure 3b). The sample (BN5) retrieved at this point shows a discrete compaction band that had propagated from the notch toward the central axis. In the third stage multiple episodic drops of the axial force were accompanied by concomitant surges in AE (Figure 3c). The deformed sample (BN1) has an array of several compaction bands that had propagated across the midsection subperpendicular to the axial force.

[16] To investigate the influence of pressure, we conducted additional experiments at lower and higher pressures. Figures 4a and 4b show the axial force and AE rate as functions of displacement for P_c = 250 and 350 MPa, respectively. The mechanical and AE data at these two pressures are qualitatively similar to those obtained by *Vajdova and Wong* [2003] at the intermediate pressure of 300 MPa (Figure 3c). The failure modes as revealed in the thin sections of the samples BN9 and BN8 deformed well into the third stage (in Figures 4a and 4b, insets) were also similar in that several subparallel compaction bands had developed.

[17] Following *Vajdova and Wong* [2003], the nominal mean stress P_o and differential stress Q_o corresponding to the onset of compactive yield at the notch tip were determined from the axial force value at which the force-
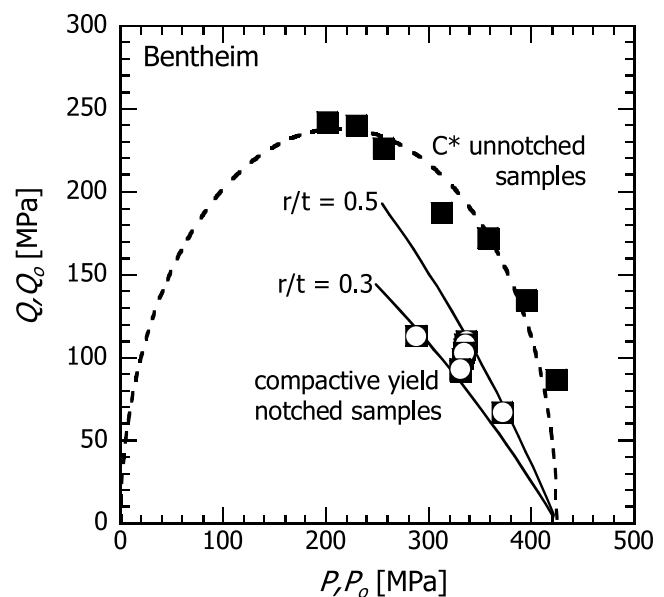

Figure 5. Initial yield stresses for notched and unnotched samples of Bentheim sandstone. Data for the unnotched samples (solid squares) are fitted by an elliptical cap (dashed curve) for differential stress Q and effective mean stress P. The notched samples have nominal differential Q_o and nominal effective mean stresses P_o (open squares) lower than their unnotched counterparts. The solid lines show the prediction of the LEFM model for the nominal stress levels at which the process zone has developed to r/t = 0.3 and 0.5, respectively.

displacement curve became nonlinear at the end of the first stage (Table 2). Because of sample variability the nominal yield stress values determined by *Vajdova and Wong* [2003] from six duplicate experiments at 300 MPa show some

scatter. Nevertheless, when they are compared with the new yield data for the lower and higher confining pressure in the stress space in Figure 5, there is an overall trend for the nominal differential stress to decrease with increasing nominal mean stress.

[18] For reference we also show in Figure 5 the compactive yield cap corresponding to the onset of shear-enhanced compaction $C*$ for unnotched samples of dry Bentheim sandstone (identical to the solid squares shown in Figure 2a). While both sets of yield stresses map out caps with negative slopes in the stress space, the presence of the notch enhanced the local stress and induced inelastic damage to initiate at a remotely applied stress significantly lower than that for an intact sample.

3.2. Localized Failure in Berea Sandstone: Three Stages of Development

[19] Three notched samples of Berea sandstone were deformed at a single confining pressure (P_c = 200 MPa) to different stages. As shown in Figure 6, three stages of failure development associated with distinct inelastic behavior and AE activity can be identified. Similar to Bentheim sandstone, the displacement of the notched Berea sandstone sample BR6 increased linearly with axial force, and termination of the first stage was signaled by an appreciable increase of AE activity (Figure 6a) at an axial force of ~101 kN corresponding to a nominal differential stress Q_o ~ 167 MPa. In the deformed sample a damage zone was also observed in the proximity of the notch (Figure 6a, inset).

[20] In the second stage (Figure 6b), there was also an upsurge of AE activity as the displacement increased nonlinearly with axial force, until the force attained a peak and this stage terminated with a small force drop (corresponding to a nominal stress drop of ~6 MPa). In sample BR5 the axial force peaked at ~109 kN, corresponding to a nominal differential stress of ~193 MPa. Although the mechanical data and AE activity are qualitatively similar to those for Bentheim sandstone (Figure 4b), the failure mode observed in the sample (BR5) retrieved after the first stress drop is very different, containing a deformation band that propagated toward the central axis at an angle of ~55° to the axial force. One may infer from the thin section image (Figure 6b inset) that the compactant strain have localized along an approximately conical surface emanating from the notch tip.

[21] In the third stage a second drop of the axial force occurred concomitantly with another upsurge in AE (Figure 6c), and in the deformed sample (BR1) a conjugate deformation band was observed to propagate also at an angle of ~55°.
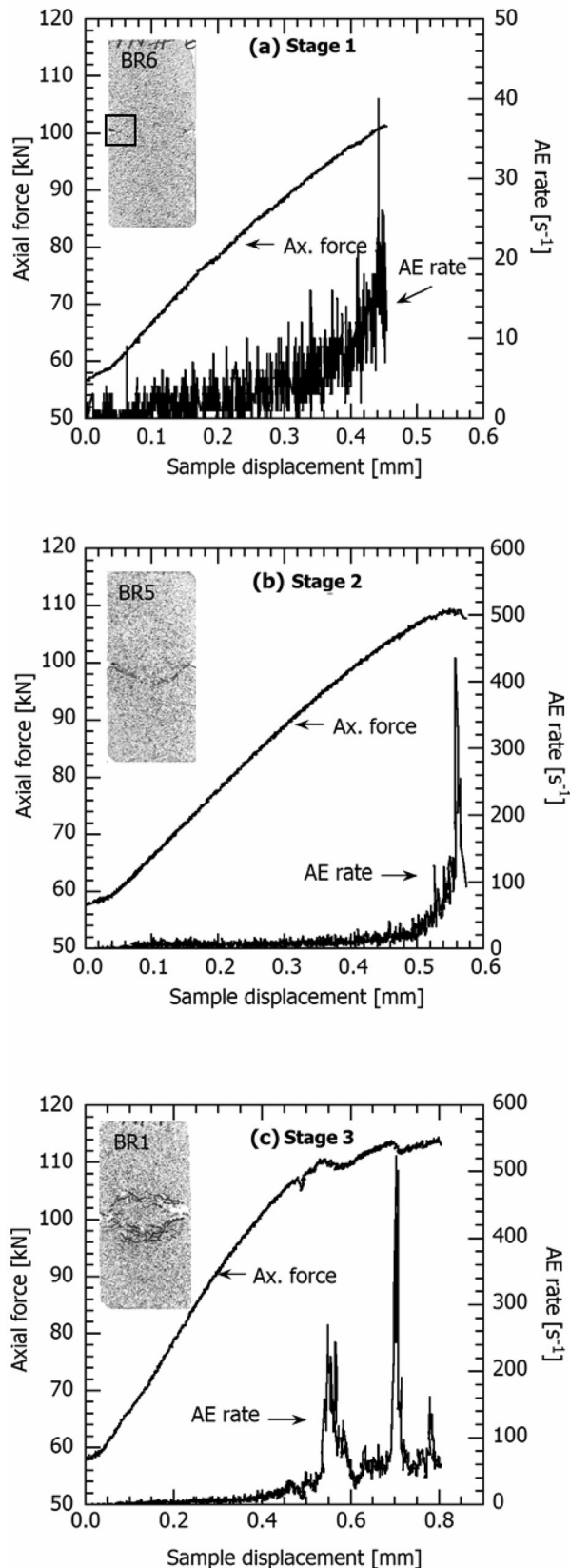
Figure 6. Axial force applied at the sample ends and AE rate as functions of axial displacement at 200 MPa confining pressure for notched samples of dry Berea sandstone loaded to various stages of compaction band development: (a) initial yield, (b) full extension of a diffuse compaction band, and (c) development of a second diffuse compaction band. Insets are thin sections of the deformed sample that show deformation bands emanating from the notch. The rectangle marks the section of sample BR6 shown in detail in Figure 9c.
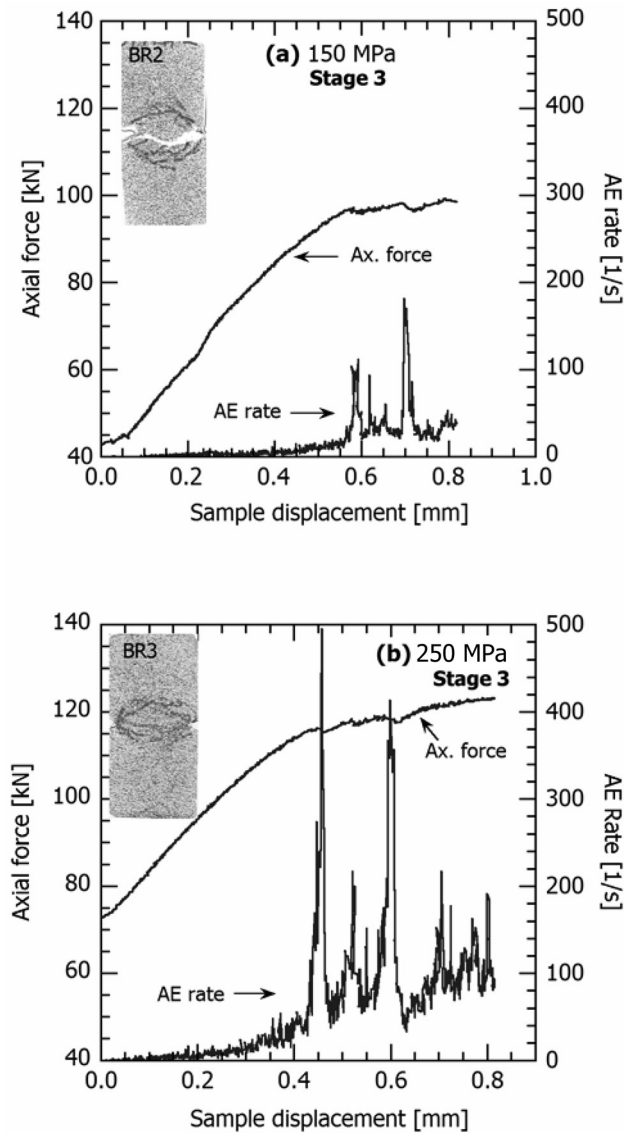
Figure 7. Axial force applied at the sample ends and AE as a function of axial displacement for notched samples of Berea sandstone deformed to stage 3 at confining pressures: (a) 150 MPa and (b) 250 MPa. Insets are thin sections of the sample showing conjugate diffuse bands at the midsection.

3.3. Berea Sandstone: Influence of Pressure on Yield Stress and Failure Mode

[22] To examine the effect of pressure, two notched Berea sandstone samples were deformed at confining pressures of 150 and 250 MPa, respectively. The mechanical and AE data at these two pressures shown in Figure 7 are qualitatively similar to those at the intermediate pressure of 200 MPa (Figure 6c). The failure modes were also similar in that conjugate deformation bands inclined at angles of ~55° to the axial force had developed in samples BR2 and BR3 which were deformed well into the third stage (Figures 7a and 7b insets). Two differences between the Berea and Bentheim sandstones in AE activity should be noted. First, in Berea sandstone the overall hardening trend in each experiment was typically punctuated by two small force

drops associated with two pronounced surges in AE rate, but some smaller AE surges were also recorded. In contrast, multiple stress drops and AE surges (of similar amplitudes) were commonly observed in Bentheim sandstone. Second, the characteristic time associated with an AE surge in Berea sandstone was ~30 s, appreciably longer than the duration of ~10 s observed in Bentheim sandstone.

[23] As before, critical values of P_o and Q_o corresponding to the initiation of compactive yield at the notch tip were determined from the onset of nonlinearity in the axial force-displacement curves. In Figure 8 we show these critical stresses along with the compactive yield cap of *Baud et al.* [2000] for the onset of shear-enhanced compaction C^* in unnotched samples of dry Berea sandstone (identical to the solid circles shown in Figure 2b) for reference. As in the Bentheim sandstone there is an overall trend for the nominal differential stress to decrease with increasing nominal mean stress, and the presence of the notch enhanced the local stress and induced inelastic damage to initiate at a remotely applied stress significantly lower than that for an unnotched sample.

4. Initiation of Compactive Yield at the Notch Tip

[24] Our optical microscope observations show that in both sandstones, the initiation and propagation of strain localization develop in three stages manifested by distinct signatures in force drop and AE activity. As far as the initiation stage is concerned, the micromechanical attributes
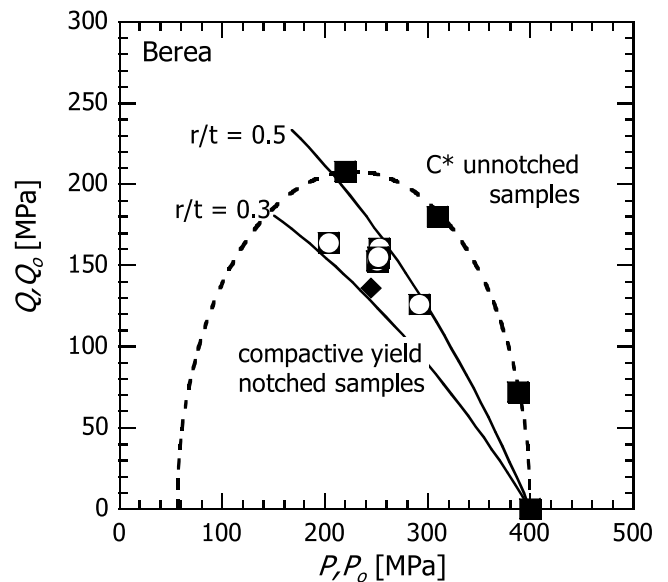

Figure 8. Initial yield stresses for notched and unnotched samples of dry Berea sandstone. Data for the unnotched samples (solid squares) are fitted by an elliptical cap (dashed curve) for differential stress Q and effective mean stress P. The notched samples have nominal differential Q_o and nominal effective mean stresses P_o (open squares) lower than the dry unnotched samples. The solid lines show the prediction of the LEFM model for the nominal stress levels at which the process zone has developed to $r/t = 0.3$ and 0.5, respectively. Also included is the initial yield stress for a water saturated notched sample (diamond) deformed at $P_c - p_p = 200$ MPa.
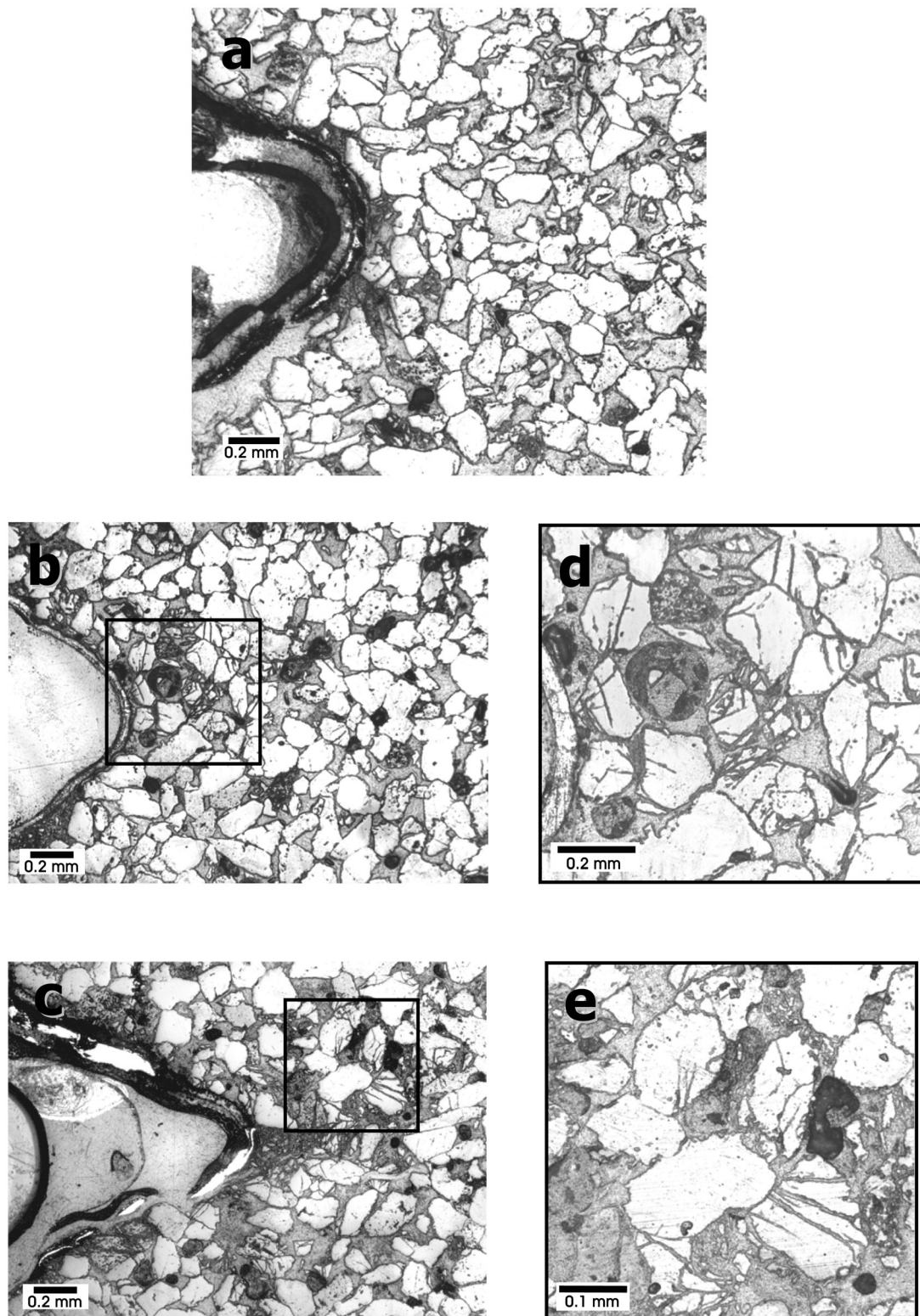
Figure 9. (a) Micrograph of a relatively intact notch area in Bentheim sandstone sample BN3. Note that there are very few intragranular cracks. The development of a process zone spanning three to four grains in (b) Bentheim sandstone sample BN7 and (c) Berea sandstone BR6, both deformed to stage 1. The rectangles mark areas containing intragranular cracking with morphology indicative of Hertzian fracturing shown in detail for samples (d) BN7 and (e) BR6.
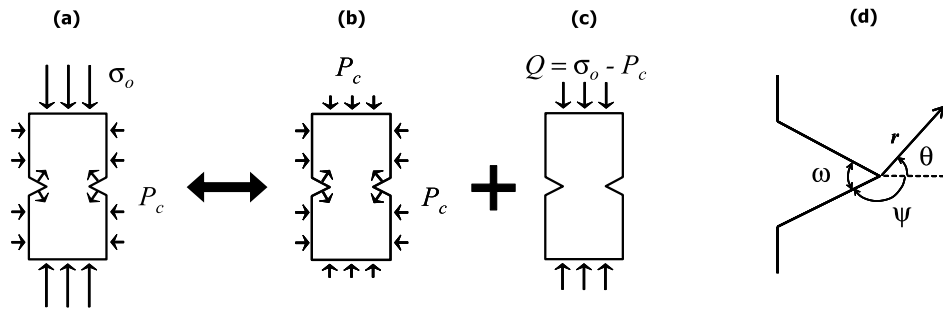
Figure 10. (a) Axisymmetric loading configuration for our notched sample, which can be represented by the superposition of two stress fields: (b) uniform hydrostatic pressure and (c) uniaxial compression. (d) Polar coordinate system near the tip of a finite angle notch.

in both sandstones are rather similar. However, since the apparent damage in this early stage tends to be highly localized near the notch, the question arises as to whether such deformation features were actually artifacts from sample preparation when the notch was machined into the cylindrical core, rather than from the stress concentration during loading. To address this question, in Figure 9a we show a micrograph from the Bentheim sandstone sample BN3. This is the sample at a confining pressure of 300 MPa that experienced the lowest axial load. A thin section of the whole sample was presented by *Vajdova and Wong* [2003, Figure 3a, inset], who showed a damage zone that had initiated near one side of the notched sample while the other side remained relatively intact. In Figure 9a we show in higher magnification the grains near the relatively intact side of the notch in BN3. Except for a few in the immediate proximity of the notch that were plucked out, most of the grains remained bonded to one another. The overall crack density was relatively low, indicating that the damage from notch sample preparation was very slight. None of the grains on this micrograph had multiple intragranular cracks emanating from grain contacts with a morphology indicative of a Hertzian fracture process that is typically associated with compactant failure [*Menéndez et al.*, 1996].

[25] In contrast, damage in the sample BN7 had localized near both sides of the notch as observed in the thin section. Figure 9b presents details near a tip, showing several grains ahead of the notch that had been crushed by Hertzian fractures. A comparison of Figure 9b with Figure 9c highlights the similarity in spatial distribution of damage in the vicinity of the notch tips of the Bentheim (BN7) and Berea (BR6) sandstone samples, both deformed to just beyond the onset of nonlinearity in the force-displacement curve and the first upsurge of AE activity. Damage in these two samples had localized near both sides of the notches. In each sample deformed to stage 1 a cluster of grains with Hertzian fractures were observed in the vicinity of the notch tip, and typically such damage would propagate from the tip over three to four grains. Figures 9d and 9e illustrate the morphology of such intragranular cracking in Bentheim and Berea sandstones, respectively, in areas at a distance of about three grain diameters from the notch tip.

[26] Since the mechanical response was linear before the onset of yield at the notch tip, as a first-order description of the initiation of compactive yield at the notch tip we

developed a micromechanical model on the basis of linear elastic fracture mechanics (LEFM). Given that the geometric attributes of the damage zones seem to be similar we expect the initiation model to apply to both sandstones.

4.1. Stress Intensity at the Notch Tip

[27] The specimen configuration and boundary conditions are illustrated in Figure 10a. The circumferentially notched cylinder has maximum and minimum diameters D and d (Figure 1), respectively and the V-shaped notch encloses the angle ω. The lateral surface of the cylinder and the notch surface are subjected to a normal stress P_c, while the two end surfaces are subjected to a nominal axial stress $\sigma_o \geq P_c$. We will first consider the stress fields for the two sets of loading conditions shown in Figures 10b and 10c, and then by linear superposition arrive at the notch tip stresses pertinent to our experimental conditions. We will use the polar coordinate system shown in Figure 10d. The overall objective of the yield initiation model is to derive the asymptotic stress field (as a function of r and θ) in the vicinity of the V notch (for a given notch angle ω) and to map out the locations at which the stress field satisfies the compactive yield condition. While the mathematical analysis for a finite ω value is quite involved, it is much simpler in the limiting case of a crack (with $\omega \to 0$) for which analytical expressions can be derived by slight modification of standard LEFM results. Furthermore, since the spatial distribution of the stress concentrations for a broad range of acute values of ω are qualitatively similar to that for $\omega \to 0$ many key features of the mechanics can be captured by considering the analytic results for the limiting case of a crack. Accordingly we will first consider this limiting case before presenting the more general results for an arbitrary notch angle ω.

[28] Since the first set of loading corresponds to a uniform hydrostatic pressure P_c applied to the external surfaces of the cylinder and notch, it results simply in a uniform stress field $\sigma_{ij}^I = P_c \delta_{ij}$. The second set of loading corresponds to a compressive stress $Q_o = \sigma_o - P_c$ applied uniformly on the end faces. If the axial loading were tensile, then this problem would be identical to the configuration widely used in engineering fracture mechanics. Extensive analyses of the mode I stress intensity factor are available and these results can be modified to derive the stress field σ_{ij}^{II} for the problem in Figure 10c. The mathematical details are summarized in Appendix A.

[29] From LEFM [e.g., *Paris and Sih*, 1965; *Lawn*, 1993] it is known that the asymptotic stress field near the crack tip is given by the following plane strain expressions:

$$\sigma_{rr}^{II}(r,\theta) = \frac{K_I}{\sqrt{2\pi r}} f_{rr}(\theta) \tag{1a}$$

$$\sigma_{\theta\theta}^{II}(r,\theta) = \frac{K_I}{\sqrt{2\pi r}} f_{\theta\theta}(\theta) \tag{1b}$$

$$\sigma_{r\theta}^{II}(r,\theta) = \frac{K_I}{\sqrt{2\pi r}} f_{r\theta}(\theta) \tag{1c}$$

$$\sigma_{zz}^{II}(r,\theta) = \upsilon\left(\sigma_{rr}^{II} + \sigma_{\theta\theta}^{II}\right) = \frac{\upsilon K_I}{\sqrt{2\pi r}}[f_{rr}(\theta) + f_{\theta\theta}(\theta)] \tag{1d}$$

where K_I is the mode I stress intensity factor, υ is Poisson's ratio, and the angular functions are given by

$$f_{rr}(\theta) = \cos\frac{\theta}{2}\left[1 + \sin^2\frac{\theta}{2}\right] \tag{2a}$$

$$f_{\theta\theta}(\theta) = \cos^3\frac{\theta}{2} \tag{2b}$$

$$f_{r\theta}(\theta) = \sin\frac{\theta}{2}\cos^2\frac{\theta}{2} \tag{2c}$$

For a circumferentially cracked sample under the uniaxial loading shown in Figure 10c, the stress intensity factor can be calculated according to *Benthem and Koiter*'s [1973] interpolation formula

$$K_I = (\sigma_o - P_c)\sqrt{\pi t}\frac{(1 + 0.5\eta + 0.375\eta^2 - 0.363\eta^3 + 0.731\eta^4)}{2\eta^{3/2}} \tag{3}$$

with the ratio $\eta = d/D$ and notch depth $t = (D - d)/2$ (Figure 1).

[30] By superposing the hydrostatic stress field $\sigma_{ij}^I = P_c\delta_{ij}$ and asymptotic values for σ_{ij}^{II} as given in equation (1) we obtain the stress field due to the axisymmetric compression shown in Figure 10a

$$\sigma_{rr}(r,\theta) = \frac{K_I}{\sqrt{2\pi r}} f_{rr}(\theta) + P_c \tag{4a}$$

$$\sigma_{\theta\theta}(r,\theta) = \frac{K_I}{\sqrt{2\pi r}} f_{\theta\theta}(\theta) + P_c \tag{4b}$$

$$\sigma_{r\theta}(r,\theta) = \frac{K_I}{\sqrt{2\pi r}} f_{r\theta}(\theta) \tag{4c}$$

$$\sigma_{zz}(r,\theta) = \frac{\upsilon K_I}{\sqrt{2\pi r}}[f_{rr}(\theta) + f_{\theta\theta}(\theta)] + P_c \tag{4d}$$

[31] As expected from a LEFM model, the asymptotic stresses have an inverse square root singularity, and accordingly they decay rapidly with increasing radial distance from the crack tip. However, the stress field in this case is somewhat different from that in conventional LEFM applications in that the stresses are not tensile but compactive. It should also be noted that the confining pressure explicitly appears in the three normal stresses, which implies that the compactive yield behavior will be pressure-dependent as observed in our experiments (Figures 5 and 8). In particular, this pressure effect is expected to be important at some distance away from the crack tip where the singular stress magnitude decreases to be comparable to P_c.

[32] As elaborated in Appendix A, the crack solution above can be generalized to a notch with a finite inclusion angle ω after accounting for three effects. First, while the crack tip stresses in equation (1), are associated with an inverse square root singularity, the asymptotic stresses at the tip of a generic notch are proportional to r^λ with a singularity characterized by the exponent λ which decreases from a value of -0.5 to -0.456 as the angle ω increases from 0 to $\pi/2$. Second, the angular functions (given by equation A5), depend on λ, involving algebraic expressions that are more complicated than equation (2). Third, the stress intensity factor K_λ (given by equation (A7)) is somewhat higher than that given by (3).

4.2. Compactive Yield Criterion and Geometry of Process Zone

[33] When stresses in the vicinity of the crack tip attain the critical values specified by an appropriate yield criterion, compactive yield will initiate and spread over a process zone. Following *Wong et al.* [1997], we consider the yield function shown to be applicable to many porous sandstones:

$$f(\sigma_{ij}) = \frac{(I_1/(3P^*) - \gamma)^2}{(1 - \gamma)^2} + \frac{(\sqrt{3J_2}/P^*)^2}{\delta^2} - 1 \tag{5}$$

where I_1 and J_2 denote the first and second stress invariants given by

$$I_1(r,\theta) = \sigma_{zz} + \sigma_{rr} + \sigma_{\theta\theta} = \frac{(1 + \upsilon)K_I}{\sqrt{2\pi r}}[f_{rr} + f_{\theta\theta}] + 3P_c \tag{6a}$$

$$\begin{aligned}J_2(r,\theta) &= \left[(\sigma_{rr} - \sigma_{\theta\theta})^2 + (\sigma_{zz} - \sigma_{rr})^2 + (\sigma_{zz} - \sigma_{\theta\theta})^2\right]/6 + \sigma_{r\theta}^2 \\ &= \frac{K_I^2}{2\pi r}\left\{f_{r\theta}^2 + \frac{(f_{rr} - f_{\theta\theta})^2 + (\upsilon f_{\theta\theta} - (1 - \upsilon)f_{rr})^2 + (\upsilon f_{rr} - (1 - \upsilon)f_{\theta\theta})^2}{6}\right\}\end{aligned} \tag{6b}$$

for the axisymmetric stress field in equation (4). Compactive yield is considered to develop if $f(\sigma_{ij}) \geq 0$. Under hydrostatic loading the yield condition is simply $I_1/3 \geq P^*$, attained when the applied pressure exceeds the critical value P^*. The yield envelope $f(\sigma_{ij}) = 0$ can be interpreted as an elliptical cap with aspect ratio $(1 - \gamma)/\delta$ and center located at $(\gamma P^*, 0)$ in the stress space with coordinates given by $I_1/3$ and $\sqrt{3J_2}$.

[34] The yield function (5) involves three parameters determined by fitting laboratory data for the initial yield stresses. In a hydrostatic test, P^* is identified with the critical pressure for the onset of pore collapse and grain crushing, manifested by an inflection point in the hydrostat and surge of AE activity. In porous sandstones the grain crushing pressure was observed to decrease with increasing grain size and porosity in accordance with a Hertzian fracture model [Zhang et al., 1990a]. For nominally dry samples of Bentheim and Berea sandstones, the P^* values have been determined to be 390 and 400 MPa, respectively [Baud et al., 2000; Klein et al., 2001].

[35] For an unnotched sample under triaxial compression the stress invariants are related to the mean and differential stresses according to $I_1/3 = P = (\sigma_1 + 2\sigma_3)/3$ and $\sqrt{3J_2} = Q = \sigma_1 - \sigma_3$. Hence laboratory data for the mean and differential stresses at the onset of shear-enhanced compaction in an unnotched sample can be fitted to an elliptical cap to constrain the two other yield parameters γ and δ. In their analysis of data for 7 sandstones with porosities ranging from 14% to 35%, Wong et al. [1997] observed that while γ has a value of $\sim$0.5, the other parameter δ ranges from 0.5 to 0.7. Corresponding to the elliptical caps that fit the data (the dashed curves) in Figures 5 and 8, the appropriate parameters are $\gamma = 0.50$ and $\delta = 0.56$ for Bentheim sandstone and $\gamma = 0.57$ and $\delta = 0.52$ for Berea sandstone.

[36] We compile in Table 2 the nominal axial stress σ_o at the onset of nonlinearity in the force-displacement curve and AE surge as a function of the confining pressure P_c. The corresponding values of nominal mean stress P_o and nominal differential stress Q_o are plotted in Figures 5 and 8. The geometric configuration of our notched sample is such that $\eta = d/D = 0.78$, so that the stress intensity factor from equation (3) is $K_I = 1.243(\sigma_o - P_c)\sqrt{\pi t}$ with $t = 2$ mm. We assumed a Poisson's ratio of $\upsilon = 0.2$, in accordance with our unpublished mechanical data for unnotched samples of both sandstones in the elastic regime over a broad range of pressures. For each pair of σ_o and P_c, the K_I was evaluated and then substituted into equations (6a) and (6b) to obtain the two stress invariants and into equation (5) to obtain the yield function $f(I_1 (r, \theta), J_2 (r, \theta))$. We then solved for the root of this yield function to map out the (r, θ) contour along which $f = 0$ (Figures 11a and 12a). Such a contour encloses a region of compactant damage that satisfies the yield condition $f \geq 0$, which will be referred to as the "compactive process zone".

[37] As elaborated in Appendix A, the stress intensity factor for our V notch is given by $K_\lambda = 1.337(\sigma_o - P_c)\sqrt{\pi} t^{0.492}$ with $t = 2$ mm, and a more involved calculation can be performed to determine the corresponding contours for a V notch with a finite ω value different from zero at nominal stress levels the same as those compiled in Table 2. The numerical results show that the overall behavior associated with initial yield is relatively insensitive to ω for a wide range of acute values we considered. In particular the spatial extent of the compactive yield in our notched samples (with an inclusion angle $\omega = 53.1°$) as shown in Figures 11b and 12b is almost identical to that for a sharp crack (with $\omega = 0$). This arises from a trade-off between a somewhat weaker singularity in the asymptotic stresses and slight enhancement of the stress

intensity factor at the tip of a finite angle notch relative to that at the tip of a crack. Consequently, the simpler analytic expressions for a sharp crack are considered to be adequate for calculating the near-tip stress field and analyzing the initial yield behavior in the compactive process zone.

[38] At the stress levels corresponding to the onset of AE activity and nonlinearity in the force-displacement curve, our LEFM model predicts that localized compactive yield has indeed developed in a process zone emanating from the notch tip over a distance ranging from 0.3 to 0.5 of the notch depth t (i.e., 0.6–1.0 mm) in both sandstones. This spatial extent corresponds to approximately 3–4 times the average grain size (Table 1), in reasonable agreement with our microstructural observations on the spatial distribution of damage and grain crushing in the vicinity of the notch tip presented in Figure 9. In the context of our continuum model for compactive yield in a polycrystalline rock, this would represent the linear dimension of a representative element volume. The process zone in Berea sandstone is predicted to extend to somewhat longer distances from the tip than in the Bentheim sandstone.

[39] The LEFM model predicts that the nominal differential stress for the onset of yield decreases with increasing nominal mean stress. To illustrate this effect, we calculated the nominal stresses at which the process zone extends to fixed distances ($r/t = 0.3$ and 0.5) ahead of a crack tip (at $\theta = 0$), shown as thick solid curves in Figures 5 and 8. It can be seen that our data for the nominal stresses at the onset of yield are bracketed by the two curves. The model also indicates a slight expansion of the process zone with increasing pressure (Figures 11 and 12), but such an effect can easily be masked by the variability among samples. Since we only retrieved samples at the onset of compactive yield at a single pressure for each sandstone, we do not have the necessary microstructural observations to investigate this issue.

4.3. Stress Path and Preferential Enhancement of the Mean Stress at the Notch Tip

[40] After the local stresses have attained the critical values associated with the yield cap, the subsequent development of compactive failure may involve a spectrum of modes depending on the local mean stress condition. Although the above analysis quantifies the spatial extent of the compactive process zone, it does not specify the failure modes that may be activated. However, the answer to this question is not straightforward since the stress paths in the vicinity of the notch tip depend on the angle θ. This complication is illustrated in Figures 13a and 13b for the Bentheim sandstone (BN5) and in Figures 14a and 14b for the Berea sandstone (BR2) sample, with stress paths calculated using the LEFM model for a crack and finite angle notch, respectively. If the confining pressure P_c is maintained constant while increasing the nominal differential stress, the stress path at the proximity of the notch tip is given by

$$\frac{I_1}{3} = P_c + \frac{\sqrt{3J_2}}{k} \tag{7}$$

Bentheim sandstone
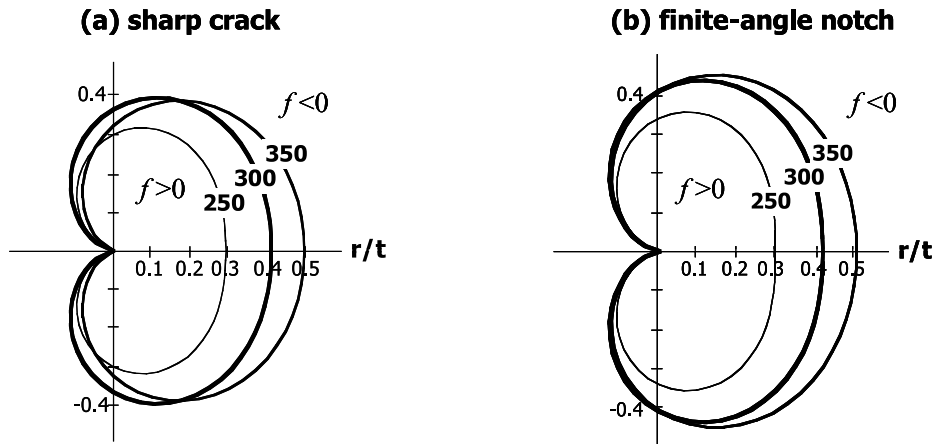
(a) sharp crack

(b) finite-angle notch

Figure 11. Geometry of the process zone in Bentheim sandstone for (a) sharp crack and (b) our finite angle notch ($\omega = 53.1°$) as predicted by our LEFM model. The contours represent the boundary of the process zone where the compactive yield criterion $f = 0$ is satisfied for $P_c = 250$, 300, and 350 MPa. The notch is located on the left side of the process zone with the tip at $r = 0$ as shown in Figure 10d.

where k corresponds to the slope of a stress path plotted in terms of $\sqrt{3J_2}$ versus $I_1/3$, or equivalently the differential stress Q versus mean stress P in axisymmetric compression. For an unnotched sample compressed triaxially at a fixed confining pressure this slope is given by $k = 3$. Analogously the nominal stresses for a notched sample also follow a path with $k = 3$. It can be seen from equations (6a) and (6b) that

both $I_1/3 - P_c$ and $\sqrt{3J_2}$ are proportional to $r^{-1/2}$, and therefore $k = \sqrt{3J_2}/(I_1/3 - P_c)$ is independent of r and depends solely on θ.

[41] Our calculations show that while the presence of a notch enhances the local stresses, the enhancement of the mean stress is appreciably higher than that of the deviatoric stress, so that the slopes of the stress paths near the
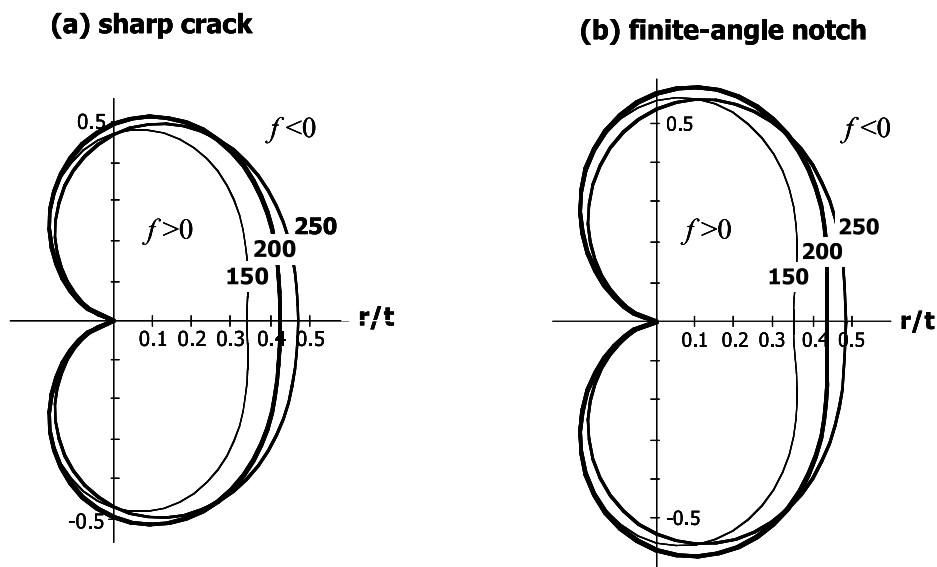
Berea sandstone

(a) sharp crack

(b) finite-angle notch

Figure 12. Geometry of the process zones in Berea sandstone for (a) sharp crack and (b) our finite angle notch ($\omega = 53.1°$) as predicted by our LEFM model. The contours represent the boundary of the process zone where the compactive yield criterion $f = 0$ is satisfied for $P_c = 150$, 200, and 250 MPa. The notch is located on the left side of the process zone with the tip at $r = 0$ as shown in Figure 10d.
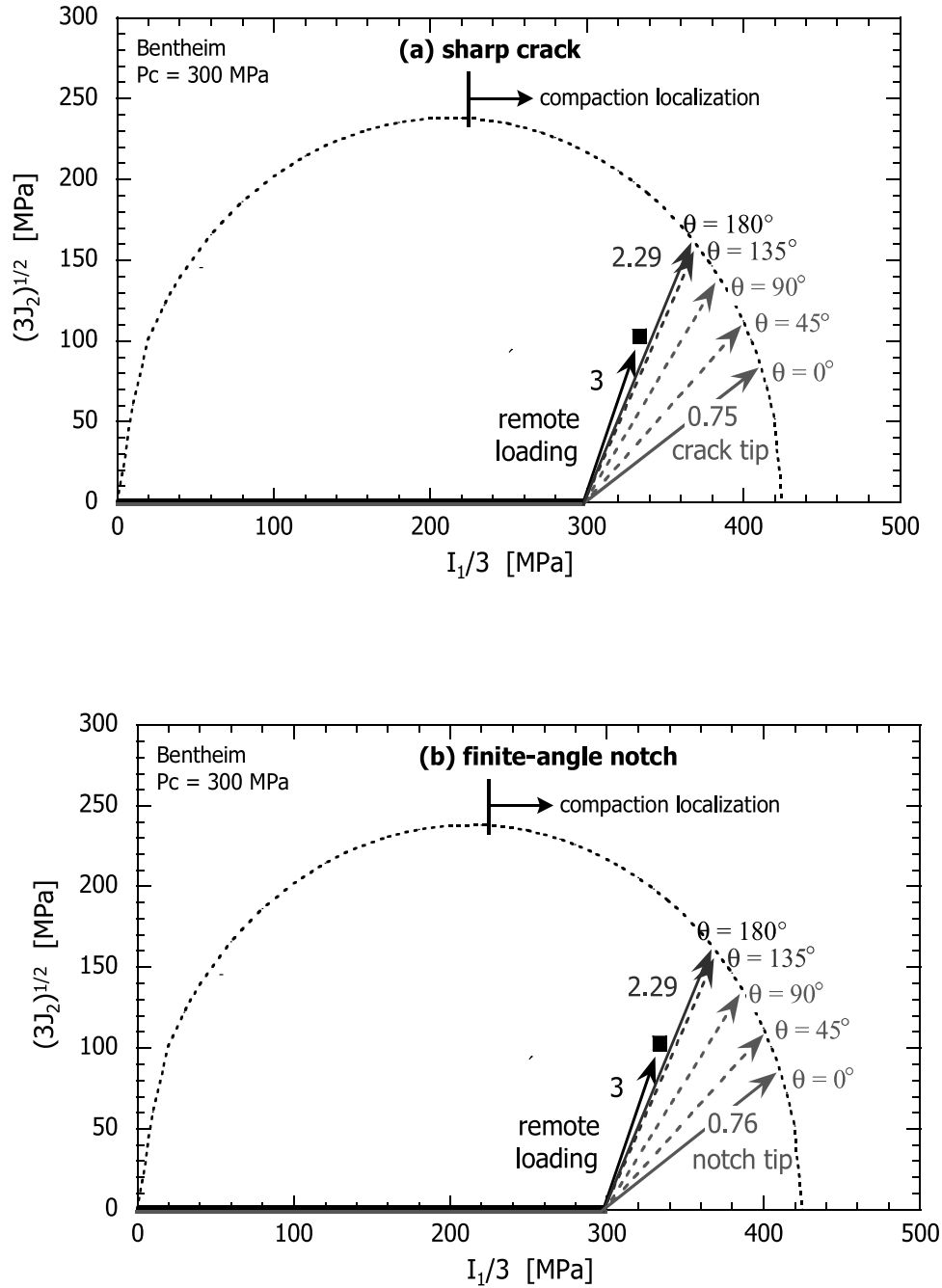
Figure 13. Stress paths for different values of θ (as depicted in Figure 10d) near the tip of (a) sharp crack and (b) finite angle notch for Bentheim sample BN5. The vertical and horizontal axes are the differential stress and effective mean stress, respectively, expressed in terms of the stress invariants. The dashed line is the compactive yield envelope for unnotched samples from Figure 5. For reference the remote loading path with slope $k = 3$ is also shown.

tip are generally lower than the nominal value of 3. Such a preferential enhancement of mean stress increases with decreasing angle θ, so that for a crack the maximum and minimum values of the slope k are attained when $\theta = \pi$ and $\theta = 0$, respectively (Figures 13a and 14a). These extremal conditions can be derived analytically. For $\theta = 0$ we observe from equations (1) and (2), that $\sigma_{\theta r}^{II} = 0$, $\sigma_{rr}^{II} = \sigma_{\theta\theta}^{II}$ and $\sigma_{zz}^{II} = \upsilon\,(\sigma_{\theta\theta}^{II} + \sigma_{rr}^{II}) = 2\,\upsilon\sigma_{rr}^{II}$, and on substituting into

equation (4), we obtain $\sigma_{rr} = \sigma_{\theta\theta} = \sigma_{rr}^{II} + P_c$ and $\sigma_{zz} = 2\upsilon\sigma_{rr}^{II} + P_c$ which imply that $I_1 = 2(1 + \upsilon)\sigma_{rr}^{II} + 3P_c$ and $\sqrt{3J_2} = (1 - 2\upsilon)\,\sigma_{rr}^{II}$. Comparing these results with equation (7), we derive that the minimum slope of the crack tip stress path is

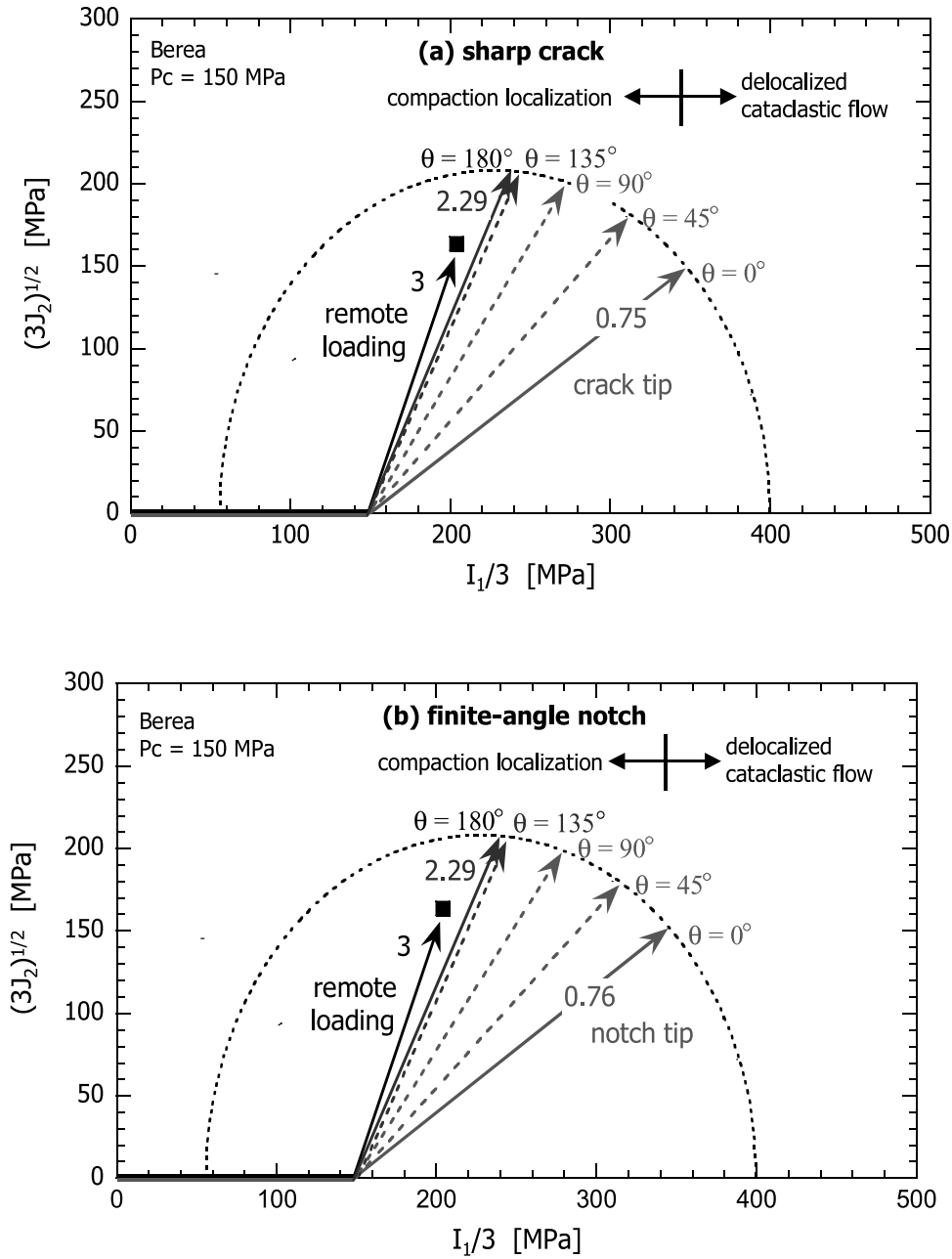$$k_{\min} = \frac{3(1 - 2\upsilon)}{2(1 + \upsilon)} \qquad (8a)$$

Figure 14. Stress paths for different values of θ (as depicted in Figure 10d) near the tip of (a) sharp crack and (b) finite angle notch for Berea sample BR2. The vertical and horizontal axes are the differential stress and effective mean stress, respectively, expressed in terms of the stress invariants. The dashed line is the compactive yield envelope for unnotched samples from Figure 8. For reference the remote loading path with slope $k = 3$ is also shown.

In Appendix A we performed a similar calculation for a finite angle notch to arrive at

$$k_{min} = \frac{3}{4(1 + \upsilon)} \left\{ 3\lambda^2 \left[1 - \frac{\sin \lambda\psi}{\sin(\lambda + 2)\psi} \right]^2 + 4(1 - 2\upsilon)^2 \right\}^{1/2}$$

(8b)

where $\psi = \pi - \omega/2$ (Figure 10d). The term inside the square bracket would vanish for a crack (with $\psi = \pi$ and $\lambda = -0.5$), in which case equation (8b) reduces to (8a). For our samples we have $\upsilon = 0.2$, $\psi = 153.4°$ and $\lambda = -0.456$ and therefore the minimum slopes according to equations (8a) and (8b) are $k_{min} = 0.75$ and 0.76, respectively. The almost identical slopes again illustrate that the crack solution represents a very good approximation for a notch with an acute inclusion angle.

[42] As for the maximum slope k_{max} it depends only on Poisson's ratio. As discussed in Appendix A, the boundary conditions require that the asymptotic stresses $\sigma_{\theta\theta}^{II}$ and $\sigma_{r\theta}^{II}$
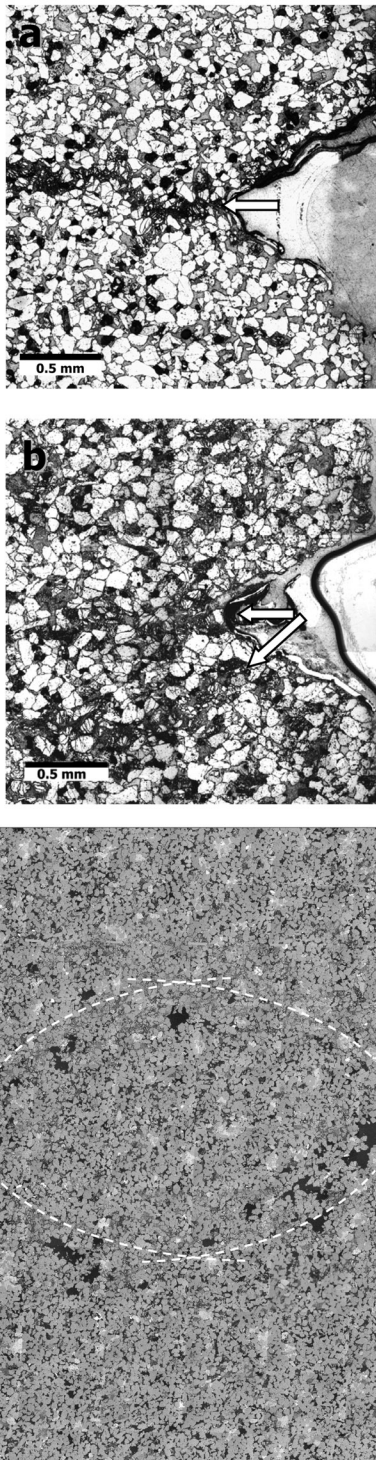
Figure 15. (a) Propagation of localization in Bentheim sandstone sample BN5 deformed to stage 2. Note that the discrete compaction band that cuts across the sample is relatively straight with a width of two to three grains. (b) Berea sandstone sample BR5 deformed to stage 2. The longer arrow indicates a diffuse band at 55° with respect to σ_1, while the short arrow point to a smaller band oriented subperpendicular to σ_1. (c) Conjugate deformation bands in sample BR1 deformed to stage 3. An approximately elliptical cross section was mapped out in a mosaic of backscattered SEM micrographs.

vanish on the surfaces of the notch, and therefore for $\theta = \psi$ the only nonzero stress components are σ_{rr}^{II} and $\sigma_{zz}^{II} = \upsilon\sigma_{rr}^{II}$. On substituting into equation (4) we obtain $\sigma_{\theta\theta} = P_c$, $\sigma_{rr} = \sigma_{rr}^{II} + P_c$, and $\sigma_{zz} = \upsilon\sigma_{rr}^{II} + P_c$, which imply that $I_1 = (1 + \upsilon)\sigma_{rr}^{II} + 3P_c$ and $\sqrt{3J_2} = \sqrt{(1 - \upsilon + \upsilon^2)}\sigma_{rr}^{II}$. Comparing these results with equation (7), we conclude that the maximum slope of the crack tip stress path is

$$k_{\max} = \frac{3\sqrt{(1 - \upsilon + \upsilon^2)}}{(1 + \upsilon)} \qquad (8c)$$

which has a value of 2.291 for $\upsilon = 0.2$. This result does not depend on the inclusion angle and is applicable to both finite angle notches and cracks.

[43] Although our LEFM model only applies to yielding on a small scale in a process zone extending over several grains, the results point to the broad range of local mean stresses that exist near the notch and the potential for different failure modes to be activated as a function of the angle θ during subsequent propagation of the compactant deformation. Consequently even though the two sandstones have similar behavior during the initiation stage of compactive yield, fundamental differences exist between the two in the subsequent development of strain localization in the notched samples.

5. Propagation of Compaction Localization

5.1. Microstructural Observations

[44] The Bentheim sandstone is quite unique in that over a broad range of pressure conditions compactant failure in an unnotched sample develops primarily by the propagation of discrete compaction bands subperpendicular to σ_1 (Figure 2a). This may explain why in a circumferentially notched sample the predominant mode of failure simply involved discrete compaction bands emanating from the notch tip, even though the process zone might actually involve a broad range of mean stresses (Figure 13). Typically a compaction band initiated from the notch tip and propagated along a relatively straight path, maintaining a lateral thickness of two to three grain diameters. This is illustrated in Figure 15a for the sample BN5 deformed at 300 MPa to stage 2, the microstructure of which was described in detail by *Vajdova and Wong* [2003].

[45] In contrast, the behavior in Berea sandstone is more complex. Here compactant failure in an unnotched sample develops by the transition of failure mode from conjugate shear to diffuse compaction band to delocalized cataclastic flow with increasing mean stress (Figure 2b). Consequently the broad range of mean stresses in the process zone of a notched sample may trigger the whole spectrum of failure modes. Figure 15b illustrates the complex damage distribution at the notch tip of sample BR5 deformed at 200 MPa and unloaded after the first stress drop and AE surge have terminated in the second stage. Although a primary band had propagated at a high angle of ~55° toward the sample axis, several short bands at different angles were also observed to have emanated from the process zone to a distance of up 1 mm or so.

[46] In the notched Berea sandstone sample during the third stage a conjugate band also developed so that the thin

section of sample BR1 shows an approximately elliptical band made up of a mosaic of crushed grains (Figure 15c). The lower half of this elliptical band appears to be wider and more diffuse, suggesting that it had developed during the first stress drop whereas the upper half subsequent propagated during the second. While the geometry of the conjugate bands would suggest that the inelastic failure had

involved both shear and compaction, it is difficult to quantify how they were partitioned in the intensely crushed grains.

5.2. Estimation of Compaction Energy

[47] To determine the energy required for the development of a discrete compaction band in Bentheim sandstone, *Vajdova and Wong* [2003] proposed that an integration under the curve of the differential force versus axial displacement provides a lower bound on the inelastic work W done during an experiment. Additional work due to overall volume reduction cannot be determined because it was not monitored. For sample BN5 (Figure 3b), *Vajdova and Wong* [2003] infer that the "compaction energy" G_c to develop such a band to be $>4W/(\pi d^2) \sim 16$ kJ m^{-2}. This is significantly higher than the specific surface energy on the order of 1 J m^{-2} for tensile fracture of minerals [*Atkinson and Meredith*, 1987], but interestingly comparable to the shear fracture energy for rocks under triaxial compression [*Wong*, 1982; *Lockner et al.*, 1991], possibly because both compaction band formation and shear fracture involve comminution of grains into numerous fine particles which can collectively have surface areas several orders of magnitude higher than the nominal area of the shear or compaction band. The comminution inside a compaction band and intense Hertzian fracturing in adjacent grains are illustrated by a micrograph for the Bentheim sandstone sample BN9 (Figure 16a).

[48] A similar calculation can be done using the data acquired in this study. The data of *Vajdova and Wong* [2003] showed that the first discrete band would have propagated and coalesced into a single band after the first stress drop at the termination of stage 2 (Figure 3b), corresponding to the point when the nominal differential stress had passed the first peak and decreased to a minimum (before climbing up to the next peak). When a sample was unloaded after stage 2, the unloading stiffness was observed to be approximately linear with a value close to the initial loading stiffness. By integration over such a loading-unloading cycle for samples BN9 and BN8, we determined compaction energy values of 27 and 6 kJ m^{-2}, respectively. As shown in Figure 16b, our inferred values of G_c for Bentheim sandstone increase with decreasing confining pressure. For reference we also plotted for each sample the nominal differential stresses at initial yield (compiled in Table 2) as well as those at the peak and residual levels for the first stress drop.

[49] Motivated by such laboratory data *Rudnicki and Sternlof* [2005] recently developed an energy release model for compaction band propagation using *Rice*'s [1968] J
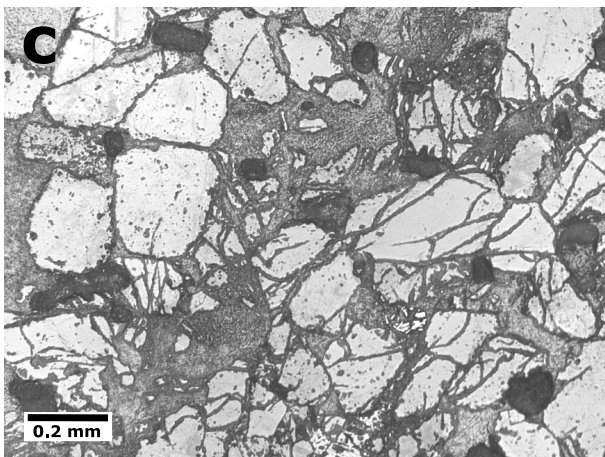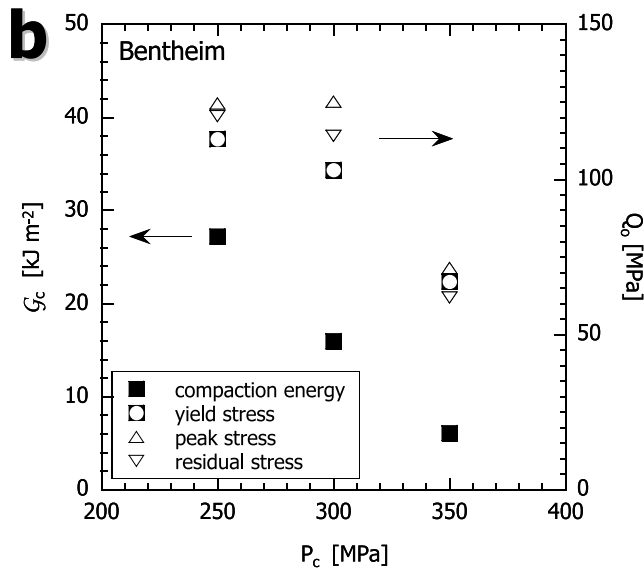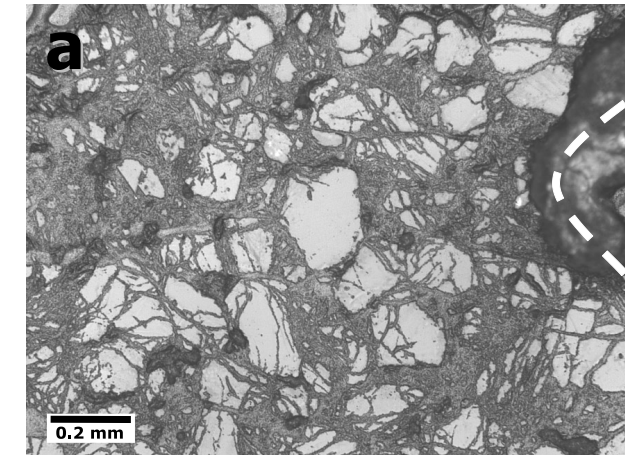
Figure 16. (a) Comminuted grains at the notch tip (outlined by the dashed white line) of sample BN9 deformed to stage 3 at P_c = 250 MPa. (b) Compaction energy G_c as a function of confining pressure for Bentheim sandstone. For reference, also plotted for each sample are the nominal differential stresses at initial yield, peak stress and residual levels for the first stress drop. (c) Damage involving comminution within a deformation band near the midsection of Berea sandstone sample BR2, deformed to stage 3 at P_c = 150 MPa. The σ_1 is oriented vertically in the micrographs.
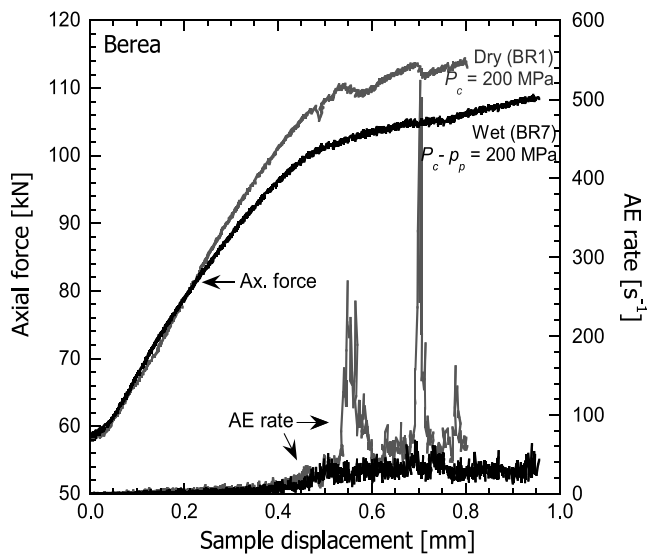
Figure 17. Mechanical and acoustic emission data for a notched Berea sandstone sample saturated in distilled water deformed at $P_c - p_p = 200$ MPa to stage 3.

integral. In their model the rock ahead of the band tip is assumed to be at a uniform stress level σ_+. As the crack tip propagates the rock yields while the normal stress initially increases to a peak σ_p and then decays to a residual level σ_-. For this scenario, *Rudnicki and Sternlof* [2005] concluded that the compaction energy can be approximated by $G_c = \sigma_+ \Delta / 2$, where Δ denotes the overall shortening of the rock mass due to the propagation of a throughgoing compaction band. In our laboratory setting σ_+, σ_p and σ_- in a notched sample can be approximated by the nominal differential stress at initial yield (compiled in Table 2), and those at the peak and residual level for the first stress drop. According to our mechanical data these stresses all decrease with increasing pressure (Figure 16b). Furthermore since the inelastic shortening Δ in the notched sample was almost constant (possibly because the compactant strain and width of bands were similar), the compaction energy G_c was observed to decrease with increasing pressure in apparent agreement with *Rudnicki and Sternlof*'s [2005] model.

[50] Using the mechanical data for BR5 (Figure 6b), we determined an energy of $G_c \sim 43$ kJ m^{-2} for the formation of a compactive deformation band in the Berea sandstone sample. The energy estimates for both sandstones are of the same order of magnitude, which is plausible since we also observed in the Berea sandstone localized damage involving comminution and Hertzian fracture (Figure 16c), qualitatively similar to that in the Bentheim sandstone (Figure 16a). However, the interpretation of the Berea sandstone value is complicated by two factors. First, the damage may arise from not only compaction but also shear. Second, the band propagated along a curvilinear path and the nominal area was estimated by assuming a semielliptical cross section (Figure 15c).

[51] To gain a deeper understanding of the mechanics of these propagation phenomena, it is necessary to advance beyond the initiation model based on LEFM and employ numerical simulations based on a more detailed constitutive

model that specifies the plastic flow law and strain hardening/softening behavior. To our knowledge, two attempts have recently been made to model the propagation of compaction localization from a notch. *Vajdova et al.* [2003] used the finite element method and their preliminary results show if strain hardening was incorporated into the constitutive model, then conjugate bands would propagate at high angles similar to our observations in Berea sandstone. However, our mechanical and microstructural data would suggest that the bands formed in succession, not as a conjugate pair as the constitutive model predicts. Given the slight geometric imperfections of a notched sample, subtle perturbations may result in the loading conditions such that one half of the Berea sandstone sample will localize before the other.

[52] *Katsman and Aharonov* [2006] used a spring network model which simulated local compactive failure by shortening the bond length, and their results show that discrete compaction bands initiated from the notch tips and propagated incrementally, similar to our observations in Bentheim sandstone. In their network model the shortening of a bond is accompanied by a local stress drop. This may explain why it could reproduce the propagation behavior in Bentheim sandstone, which typically shows an overall strain hardening punctuated by episodic stress drops [*Wong et al.*, 2001]. In contrast, the mechanical response of an intact Berea sandstone sample shows overall hardening without such transient softening cycles [*Baud et al.*, 2004].

[53] Our laboratory data and microstructural observations can provide additional constraints on these theoretical models. It seems unlikely that the fundamentally different propagation behaviors in the two sandstones can be captured in a model without appropriately accounting for the interplay of strain hardening and softening in a unified manner. Although it is beyond the scope of the present study, we consider the development of such a continuum or discrete model to be critical for elucidating the mechanics of compaction localization and its sensitivity to stress and structural heterogeneity.

5.3. Geologic Implication

[54] Recent studies have documented that a porous sandstone undergoing compaction may fail by a variety of localized or delocalized modes. In this study we demonstrate that the presence of a stress and structural heterogeneity in the form of a notch can be very effective in enhancing the local mean stress and activating a number of failure modes. To extrapolate our laboratory observations to the geologic setting, there are at least three questions to be addressed. First, although we investigated the behavior over a broad range of pressures, only two sandstones were studied. Are their behaviors representative of porous sandstones in general? Second, only nominally dry samples were investigated, but in the field the pore space of the rock is often saturated with water. Can the behavior be significantly different in the presence of a chemically reactive fluid? Third, a key feature of our sample configuration is that we introduced a circumferential notch to simulate a structural heterogeneity in the field. In what sense does the notch provide a geologic analogue and how can the mechanical data be extrapolated and scaled to field settings?

[55] The first question can partially be addressed by the many studies on unnotched sandstone samples. We selected the Bentheim and Berea sandstones because between the two the full range of compactive failure modes (including high-angle conjugate shear bands, discrete and diffuse compaction bands, and delocalized cataclastic flow) have been observed in previous work (Figure 2). While it is useful to extend the investigation to other sandstones, we believe our observations are quite representative of the spectrum of compaction localization behavior to be expected.

[56] Previous studies [e.g., *Baud et al.*, 2000] on unnotched sandstone samples have also demonstrated that although the phenomenology of compactive failure is similar in nominally dry and saturated samples, the yield stresses are somewhat lower in the presence of water. We have conducted a pilot study to investigate this water weakening effect in a notched sample of Berea sandstone. Sample BR7 was saturated in distilled water and compressed to the third stage of deformation at effective pressure of $P_{eff} = 200$ MPa ($P_c = 210$ MPa and pore pressure $p_p = 10$ MPa). The force-displacement curve has a monotonic hardening trend (Figure 17). The compactive yield stress of the wet sample ($P_o = 245$ MPa and $Q_o = 136$ MPa) is lower than the dry samples (indicated by the diamond plotted in Figure 8) but interestingly, microstructural observations show the development of conjugate deformation bands in BR7, with the spatial distribution of damage qualitatively similar to dry samples deformed to the third stage. A more comprehensive investigation extending to other sandstones over a broader range of pressures in the presence of water is desirable.

[57] Our LEFM model provides useful insights into the role of the notch in enhancing the local stress field. The initiation of compactive yield and formation of a process zone is relatively insensitive to the exact value of the notch inclusion angle, and one can simply analyze the overall behavior using analytic results from crack mechanics. However, it is critical that the fracture remains open to play a role analogous to the notch in our samples. From a variety of geophysical measurements [e.g., *Nur and Walder*, 1990] open fractures have been inferred to be present on many scales in the upper crust, providing interconnected conduits for fluid percolation [*Brace*, 1980]. It is widely appreciated that elevated fluid pressure can induce such fractures to extend in a tensile mode, and they may also coalesce to develop a shear fault [e.g., *Segall and Pollard*, 1983]. Here we demonstrate that such open fractures under compressive loading can also play an effective role in nucleating compactive failure in the form of discrete or diffuse compaction bands, as well as high-angle conjugate shear bands. This scenario may be important in the development of deformation bands and their geometric complexity in the field [e.g., *Aydin and Johnson*, 1978]. It seems that an analogous analysis may also apply to the development of borehole breakout [e.g., *Haimson*, 2003].

6. Summary and Conclusion

[58] We have demonstrated the spectrum of localized failure modes under the well defined conditions of stress concentration in the Bentheim and Berea sandstones. To investigate how compaction localization develops from a structural and stress heterogeneity, we introduced a V-shaped circumferential notch in cylindrical samples and conducted triaxial compression tests at confining pressure optimum for compactive failure. Our mechanical and microstructural data depict two phases in the development of a localized structure, the initiation and propagation.

[59] The initiation of compactive yield was marked by the onset of nonlinearity in the force-displacement curve and upsurge in acoustic emissions, corresponding to the formation of a process zone. Microstructural observations of samples recovered at the onset of inelastic behavior show a process zone extending ∼3 to 4 grains from the notch tip in both sandstones. We developed a micromechanical model using LEFM to probe the initial yield behavior and geometric attributes of the process zone. By considering the axisymmetric loading conditions in our sample configuration as the linear superposition of uniform hydrostatic pressure and a compressive uniaxial stress we arrived at an asymptotic solution for the notch tip stresses. Our model predicts localized compactive yield to occur at the notch tip in a process zone extending 0.3 to 0.5 of the notch depth, in accord with the microstructural observations. The presence of the notch enhanced the local stress and induced damage to occur at a remote stresses significantly lower than in the unnotched sample such that the critical stresses necessary for yield map out a cap with a negative slope in the stress space. Using our model, an analysis of the stress path reveals that since a broad range of mean stresses are involved various localization modes are potentially activated around the notch tip. Thus, despite similarities at initiation the subsequent growth of a localized structure is fundamentally different in the Bentheim and Berea sandstones.

[60] Beyond initiation, we observed strain localization in the Bentheim sandstone to propagate as discrete compaction bands that cut through the sample cross section with episodic force drops and as conjugate diffuse bands from the Berea sandstone accompanied by strain hardening. Microstructural observations of samples deformed within a range of confining pressures have qualitatively similar spatial distribution of damage. A calculation of the energy G_c required to develop a discrete compaction band was determined to be 6−27 kJ m^{-2} for Bentheim sandstone at confining pressures ranging from 250 to 350 MPa and ∼43 kJ m^{-2} for a compactive deformation band in Berea sandstone at confining pressure of 200 MPa.

Appendix A

[61] We consider the asymptotic stress field σ_{ij}^{II} (r, θ) in the vicinity of a notch tip under a remotely applied uniaxial stress along the z axis (Figure 10c). The notch has an inclusion angle denoted by ω (Figure 10d). *Williams* [1952] formulated an approach by which the singular stress field can be derived from an Airy stress function in the form

$$U(r, \theta) = \sum_{\lambda} r^{\lambda+2} \left[A_{\lambda} e^{i\lambda\theta} + B_{\lambda} e^{i(\lambda+2)\theta} \right] \qquad (A1)$$

where A_λ and B_λ are complex coefficients. Since the notch surfaces at $\theta = \pm\psi = \pm(\pi - \omega/2)$ are traction free (Figure 10d), the boundary conditions are

$$\sigma_{\theta\theta}^{II}(r, \pm\psi) = \frac{\partial^2 U}{\partial r^2}(r, \pm\psi) = 0 \quad (A2a)$$

$$\sigma_{r\theta}^{II}(r, \pm\psi) = -\frac{\partial}{\partial r}\left[\frac{1}{r}\frac{\partial U}{\partial \theta}(r, \pm\psi)\right] = 0 \quad (A2b)$$

On substituting (A1) into (A2a) and (A2b) we obtain two simultaneous equations in A_λ and B_λ, which have nontrivial solutions only if this determinant vanishes:

$$(\lambda + 1)\sin 2\psi + \sin 2(\lambda + 1)\psi = 0 \quad (A3)$$

To satisfy displacement continuity and give unbounded stresses near the notch tip, the eigenvalue must satisfy the condition $0 > \lambda > -1$ [*Williams*, 1952], and therefore λ characterizes the stress singularity at the notch tip. If $\psi = \pi$ we have $\lambda = -1/2$, corresponding to the inverse square root singularity for a crack.

[62] Components of the singular stress field can be written as

$$\sigma_{rr}^{II}(r, \theta) = \frac{K_\lambda}{\sqrt{2\pi}} r^\lambda f_{rr}(\theta) \quad (A4a)$$

$$\sigma_{\theta\theta}^{II}(r, \theta) = \frac{K_\lambda}{\sqrt{2\pi}} r^\lambda f_{\theta\theta}(\theta) \quad (A4b)$$

$$\sigma_{r\theta}^{II}(r, \theta) = \frac{K_\lambda}{\sqrt{2\pi}} r^\lambda f_{r\theta}(\theta) \quad (A4c)$$

$$\sigma_{zz}^{II}(r, \theta) = \upsilon(\sigma_{rr}^{II} + \sigma_{\theta\theta}^{II}) = \frac{\upsilon K_\lambda}{\sqrt{2\pi}} r^\lambda [f_{rr}(\theta) + f_{\theta\theta}(\theta)] \quad (A4d)$$

where K_λ represents an equivalent stress intensity factor such that for $\lambda = -1/2$ we have $K_\lambda = K_I$ for a mode I crack, and the angular dependence is given by

$$f_{rr}(\theta) = -(\lambda + 1)[(\lambda - 2)A_\lambda \cos \lambda\theta + (\lambda + 2)B_\lambda \cos(\lambda + 2)\theta] \quad (A5a)$$

$$f_{\theta\theta}(\theta) = (\lambda + 1)(\lambda + 2)[A_\lambda \cos \lambda\theta + B_\lambda \cos(\lambda + 2)\theta] \quad (A5b)$$

$$f_{r\theta}(\theta) = (\lambda + 1)[\lambda A_\lambda \sin \lambda\theta + (\lambda + 2)B_\lambda \sin(\lambda + 2)\theta] \quad (A5c)$$

Expressions for the coefficients A_λ and B_λ can be derived from the results of *Dunn et al.* [1997]:

$$A_\lambda = -\frac{\sin(\lambda + 2)\psi}{(\lambda + 1)[\lambda \sin \lambda\psi - (\lambda + 2)\sin(\lambda + 2)\psi]} \quad (A6a)$$

$$B_\lambda = \frac{\lambda \sin \lambda\psi}{(\lambda + 1)(\lambda + 2)[\lambda \sin \lambda\psi - (\lambda + 2)\sin(\lambda + 2)\psi]} \quad (A6b)$$

[63] *Noda and Takase* [2003] recently presented a comprehensive calculation of the equivalent stress intensity factor of a circumferentially notched sample under tension, shear and torsion. Numerical values tabulated in Noda and Takase's Table 10 (for a circumferential notch with ω ranging from $15°-90°$ at increments of $15°$) show that under tensile loading the dependence of K_λ on the diameter ratio $\eta = d/D$ is identical to the Benthem-Koiter formula (for a mode I circumferential crack with $\omega = 0$). Hence the stress intensity factor for a finite angle notch can be expressed by an equation analogous to (3):

$$K_\lambda = \xi_\lambda(\sigma_o - P_c)\sqrt{\pi}t^{-\lambda}$$
$$\cdot \frac{(1 + 0.5\eta + 0.375\eta^2 - 0.363\eta^3 + 0.731\eta^4)}{2\eta^{3/2}} \quad (A7)$$

where the ratio $\xi_\lambda = 1$ for a crack (with $\lambda = -1/2$) and its value for a notch with different value of λ can be determined by comparing the value of $K_\lambda t^\lambda/[(\sigma_o - P_c)\sqrt{\pi}]$ for the notch with that of a crack with identical η. In particular, *Noda and Takase* [2003, Table 1] compiles the values for a notch in an infinite plate, corresponding to $\eta \to 0$. Interpolation of their compiled values (for ω ranging from $15°-90°$ at increments of $15°$) gives $K_\lambda t^\lambda/[(\sigma_o - P_c)\sqrt{\pi}] = 1.205$ for $\omega = 53.1°$ (the inclusion angle for our notched samples), and since the corresponding value for a crack (with $\omega = 0$) is 1.12 (equation (3)), we determined $\xi_\lambda = 1.205/1.12 = 1.076$ for our samples. From equation (A3) we calculated the notch singularity to be $\lambda = -0.492$ for $\psi = \pi - \omega/2 = 153.5°$, and since $\eta = 0.78$ for our notched samples the stress intensity factor from equation (A7) is $K_\lambda = 1.337(\sigma_o - P_c)\sqrt{\pi}t^{0.492}$ with $t = 2$ mm.

[64] To calculate the minimum slope $k_{\min}$ of the stress path in equation (8b), we also need to derive the asymptotic stresses at $\theta = 0$, which from (A4) and (A5) are

$$\sigma_{rr}^{II}(r, 0) = -\frac{K_\lambda}{\sqrt{2\pi}} r^\lambda(\lambda + 1)[(\lambda - 2)A_\lambda + (\lambda + 2)B_\lambda] \quad (A8a)$$

$$\sigma_{\theta\theta}^{II}(r, 0) = \frac{K_\lambda}{\sqrt{2\pi}} r^\lambda(\lambda + 1)(\lambda + 2)[A_\lambda + B_\lambda] \quad (A8b)$$

$$\sigma_{zz}^{II}(r, 0) = \frac{4\upsilon K_\lambda}{\sqrt{2\pi}} r^\lambda(\lambda + 1)A_\lambda \quad (A8c)$$

and accordingly the two stress invariants are given by

$$I_1 = 3P_c + \sigma_{rr}^{II}(r, 0) + \sigma_{\theta\theta}^{II}(r, 0) + \sigma_{zz}^{II}(r, 0)$$
$$= 3P_c + \frac{4K_\lambda}{\sqrt{2\pi}} r^\lambda(1 + \upsilon)(1 + \lambda)A_\lambda \quad (A9a)$$

$$6J_2 = [\sigma_{rr}^{II}(r, 0) - \sigma_{\theta\theta}^{II}(r, 0)]^2 + [\sigma_{rr}^{II}(r, 0) - \sigma_{zz}^{II}(r, 0)]^2$$
$$+ [\sigma_{zz}^{II}(r, 0) - \sigma_{\theta\theta}^{II}(r, 0)]^2 \quad (A9b)$$
$$= \frac{K_\lambda^2}{\pi} r^{2\lambda}(1 + \lambda)^2\left\{3[\lambda A_\lambda + (\lambda + 2)B_\lambda]^2 + 4(1 - 2\upsilon)^2 A_\lambda^2\right\}$$

On substituting (A6a), (A6b) into these equations we arrive at the expression for $k_{min} = \sqrt{3J_2}/(P - P_c)$ as given in (8b).

References

Atkinson, B. K., and P. G. Meredith (1987), Experimental fracture mechanics data for rocks and minerals, in *Fracture Mechanics of Rock*, edited by B. K. Atkinson, pp. 477–525, Elsevier, New York.

Aydin, A., and A. M. Johnson (1978), Development of faults as zones of deformation bands and as slip surfaces in sandstone, *Pure Appl. Geophys.*, *116*, 931–942.

Baud, P., W. Zhu, and T.-f. Wong (2000), Failure mode and weakening effect of water on sandstone, *J. Geophys. Res.*, *105*, 16,371–16,389.

Baud, P., E. Klein, and T.-f. Wong (2004), Compaction localization in porous sandstones: Spatial evolution of damage and acoustic emission activity, *J. Struct. Geol.*, *26*, 603–624.

Benthem, J. P., and W. T. Koiter (1973), Asymptotic approximations to crack problems, in *Mechanics of Fracture I*, edited by G. C. Sih, pp. 131–178, Springer, New York.

Brace, W. F. (1980), Permeability of crystalline and argillaceous rocks, *Int. J. Rock Mech. Min. Sci.*, *17*, 241–251.

DiGiovanni, A. A., J. T. Fredrich, D. J. Holcomb, and W. A. Olsson (2000), Micromechanics of compaction in an analogue reservoir sandstone, *Proc. U.S. Rock Mech. Symp.*, *4th*, 1153–1160.

Dunn, M. L., W. Suwito, and S. Cunningham (1997), Stress intensities at notch singularities, *Eng. Fract. Mech.*, *57*, 417–430.

Haimson, B. C. (2003), Borehole breakouts in Berea sandstone reveal a new fracture mechanism, *Pure Appl. Geophys.*, *160*, 813–831.

Holcomb, D. J., and W. A. Olsson (2003), Compaction localization and fluid flow, *J. Geophys. Res.*, *108*(B6), 2290, doi:10.1029/2001JB000813.

Issen, K. A., and J. W. Rudnicki (2000), Conditions for compaction bands in porous rock, *J. Geophys. Res.*, *105*, 21,529–21,536.

Katsman, R., and E. Aharonov (2006), A study of compaction bands originating from cracks, notches, and compacted defects, *J. Struct. Eng.*, in press.

Klein, E., P. Baud, T. Reuschle, and T.-f. Wong (2001), Mechanical behaviour and failure mode of Bentheim sandstone under triaxial compression, *Phys. Chem. Earth, Part A, 26*, 21–25.

Lawn, B. (1993), *Fracture of Brittle Solids*, 2nd ed., 378 pp., Cambridge Univ. Press, New York.

Lockner, D. A., J. D. Byerlee, V. Kuksenko, A. Ponomarev, and A. Sidorin (1991), Quasi-static fault growth and shear fracture energy in granite, *Nature*, *350*, 39–42.

Menéndez, B., W. Zhu, and T.-f. Wong (1996), Micromechanics of brittle faulting and cataclastic flow in Berea sandstone, *J. Struct. Geol.*, *18*, 1–16.

Mollema, P. N., and M. A. Antonellini (1996), Compaction bands: A structural analog for anti-mode I cracks in aeolian sandstone, *Tectonophysics*, *267*, 209–228.

Noda, N.-A., and Y. Takase (2003), Generalized stress intensity factors of V-shaped notch in a round bar under torsion, tension, and bending, *Eng. Fract. Mech.*, *70*, 1447–1466.

Nur, A., and J. Walder (1990), Time-dependent hydraulics of the Earth's crust, in *The Role of Fluids in Crustal Processes*, edited by J. D. Bredehoeft and D. L. Norton, pp. 113–127, Natl. Acad. Press, Washington, D. C.

Olsson, W. A. (1999), Theoretical and experimental investigation of compaction bands in porous rock, *J. Geophys. Res.*, *104*, 7219–7228.

Olsson, W. A., and D. J. Holcomb (2000), Compaction localization in porous rock, *Geophys. Res. Lett.*, *27*, 3537–3540.

Paris, P. C., and G. C. Sih (1965), Stress analysis of cracks, in *Fracture Toughness and Its Applications*, ASTM Spec. Tech. Publ., *381*, 30–81.

Rice, J. R. (1968), Fault stress states, pore pressure distributions, and the weakness of the San Andreas fault, in *Fault Mechanics and Transport Properties of Rocks*, edited B. Evans and T.-f. Wong, pp. 475–504, Springer, New York.

Rudnicki, J. W., and K. R. Sternlof (2005), Energy release model of compaction band propagation, *Geophys. Res. Lett.*, *32*, L16303, doi:10.1029/2005GL023602.

Segall, P., and D. D. Pollard (1983), Nucleation and growth of strike-slip faults in granite, *J. Geophys. Res.*, *88*, 555–568.

Sternlof, K. R., J. R. Chapin, D. D. Pollard, and L. J. Durlofsky (2004), Permeability effects of deformation band arrays in sandstone, *AAPG Bull.*, *88*, 1315–1329.

Vajdova, V., and T. Wong (2003), Incremental propagation of discrete compaction bands: Acoustic emission and microstructural observations on circumferentially notched samples of Bentheim, *Geophys. Res. Lett.*, *30*(14), 1775, doi:10.1029/2003GL017750.

Vajdova, V., T.-f. Wong, D. E. Farrell, V. Challa, and K. A. Issen (2003), Experimental observation and numerical simulation of initiation and propagation of compaction bands in a sandstone, paper presented at 16th ASCE Engineering Mechanics Conference, Seattle, Wash.

Vajdova, V., P. Baud, and T.-f. Wong (2004), Permeability evolution during localized deformation in Bentheim sandstone, *J. Geophys. Res.*, *109*, B10406, doi:10.1029/2003JB002942.

Williams, M. L. (1952), Stress singularities resulting from various boundary conditions in angular corners of plates in extension, *J. Appl. Mech.*, *74*, 526–528.

Wong, T.-f. (1982), Shear fracture energy of Westerly granite from post-failure behavior, *J. Geophys. Res.*, *87*, 990–1000.

Wong, T.-f., C. David, and W. Zhu (1997), The transition from brittle faulting to cataclastic flow in porous sandstones: Mechanical deformation, *J. Geophys. Res.*, *102*, 3009–3025.

Wong, T.-f., P. Baud, and E. Klein (2001), Localized failure modes in a compactant porous rock, *Geophys. Res. Lett.*, *28*, 2521–2524.

Zhang, J., T.-f. Wong, and D. M. Davis (1990a), Micromechanics of pressure-induced grain crushing in porous rocks, *J. Geophys. Res.*, *95*, 341–352.

Zhang, J., T.-f. Wong, T. Yanagidani, and D. M. Davis (1990b), Pressure-induced microcracking and grain crushing in Berea and Boise sandstones: Acoustic emission and quantitative microscopy measurements, *Mech. Mater.*, *9*, 1–15.

————————————

S. Tembe, T.-f. Wong, and W. Zhu, Department of Geosciences, State University of New York at Stony Brook, Stony Brook, NY 11794, USA. (stembe@ic.sunysb.edu)

V. Vajdova, ReedHycalog, Tech Bldg., 6501 Navigation Blvd., Houston, TX 77011-0000, USA.